ARL-TR-7310 • JUN 2015

US Army Research Laboratory

Material Parameter Sensitivity of Predicted Injury in the Lower Leg

by Megan L Lynch, Samantha L Wozniak, and Adam Sokolow

NOTICES

Disclaimers

ARL-TR-7310 ● JUN 2015

US Army Research Laboratory

Material Parameter Sensitivity of Predicted Injury in the Lower Leg

by Megan L Lynch and Adam Sokolow
Weapons and Materials Research Directorate, ARL

Samantha L Wozniak
TKC Global, LLC

REPORT DOCUMENTATION PAGE

Form Approved
OMB No. 0704-0188

1. REPORT DATE *(DD-MM-YYYY)*
Jun 2015

2. REPORT TYPE
Final

3. DATES COVERED (From - To)
Dec 2013 – Mar 2014

4. TITLE AND SUBTITLE
Material Parameter Sensitivity of Predicted Injury in the Lower Leg

5a. CONTRACT NUMBER

5b. GRANT NUMBER

5c. PROGRAM ELEMENT NUMBER

6. AUTHOR(S)
Megan L Lynch, Samantha L Wozniak, and Adam Sokolow

5d. PROJECT NUMBER
AH80

5e. TASK NUMBER

5f. WORK UNIT NUMBER

7. PERFORMING ORGANIZATION NAME(S) AND ADDRESS(ES)
US Army Research Laboratory
ATTN: RDRL-WMP-B
Aberdeen Proving Ground, MD 21005-5066

8. PERFORMING ORGANIZATION REPORT NUMBER
ARL-TR-7310

9. SPONSORING/MONITORING AGENCY NAME(S) AND ADDRESS(ES)

10. SPONSOR/MONITOR'S ACRONYM(S)

11. SPONSOR/MONITOR'S REPORT NUMBER(S)

12. DISTRIBUTION/AVAILABILITY STATEMENT
Approved for public release; distribution is unlimited.

13. SUPPLEMENTARY NOTES
primary author's email: <megan.l.lynch.civ@mail.mil>.

14. ABSTRACT

This report documents the extensive work done on the lower leg finite element model, specifically on the sensitivity of injury prediction on linear elastic material parameters that are chosen within a range of values typically used for biological tissues. Using simple criteria, we predict a variety of injuries typically observed in theater. We find a strong dependence of these predicted injuries on the soft tissue properties included in our model. We also report on a potential oversensitivity in our model to predicting talus injuries. We conclude that biological variability in measured material parameters will need to be accounted for in future models.

15. SUBJECT TERMS
lower extremities, under-body blast, accelerative loading, injury prediction, finite element model

16. SECURITY CLASSIFICATION OF:			**17. LIMITATION OF ABSTRACT**	**18. NUMBER OF PAGES**	**19a. NAME OF RESPONSIBLE PERSON** Adam Sokolow
a. REPORT Unclassified	**b. ABSTRACT** Unclassified	**c. THIS PAGE** Unclassified	UU	66	**19b. TELEPHONE NUMBER (Include area code)** 410-306-2985

Standard Form 298 (Rev. 8/98)
Prescribed by ANSI Std. Z39.18

Contents

List of Figures

List of Tables

Acknowledgment

This research was supported in part by an appointment to the Postgraduate Research Participation Program at the US Army Research Lab (ARL) administered by the Oak Ridge Institute for Science and Education through an interagency agreement between the US Department of Energy and ARL.

INTENTIONALLY LEFT BLANK.

1. Introduction

Over the past decade, the use of improvised explosive devices (IEDs) by enemy forces has increased exposure among US combat vehicles and Soldiers to underbody blast (UBB) events. During such an event, explosive detonated underground causes a rapid expansion of soil and gases under a vehicle. Momentum is imparted to the vehicle hull by a combination of the expanding gases and the surrounding soil. Energy is transmitted through the hull to the internal vehicular floor that within milliseconds produces a deformation of the floor plate. These rapid deformations of the floor plate transmit significant loads to the Soldier's lower extremities and induce accelerative injury.[1,2]

Medical injury data reveals that the lower extremities are one of the most commonly injured body regions among mounted Soldiers in theater.[3–6] The current understanding of these lower extremity injuries is largely based on research within the car crash industry. However, UBB events exert forces on occupants of ground combat vehicles that are of higher magnitude, in different directions, and over a shorter duration than forces in civilian car accidents,[1,6] making these injuries and their mechanisms unique to the military population.

During Operation Enduring Freedom and Operation Iraqi Freedom more than 16,000 Soldiers were unable to return to duty due to their injuries.[7] Recent studies have shown that up to 50% of Soldiers wounded in action have sustained a lower extremity injury.[7–9] UBB-induced injuries to the lower extremities are frequently associated with fractures to multiple bones and may also involve damage to the surrounding soft tissues, nerves, and vascular network. It has been shown that for patients that have sustained multiple injuries, those with foot and ankle injuries have a greater disability score than those without foot and ankle injuries. Furthermore, those who sustained an injury to the calcaneus are associated with the highest complication rate.[8] Advances in technology have both increased the opportunities for surgeons to salvage limbs, as well as helped in the development of better prostheses for amputees. Patients who decide to salvage their lower extremities often require a longer period of rehabilitation compared to those who decide to amputate their leg.[10] To the wounded warrior, a return to high levels of physical activity is often a priority since it will affect their ability to return to full military duty. It is not uncommon for patients with salvaged limbs who have dealt with chronic infection, constant pain, or poor functional outcome to opt for elective amputation.[7,10] Understanding the mechanism that causes one injury over another is therefore important for protection design concepts.

The process of insult to injury must be well understood to effectively design protection systems that mitigate lower extremity injuries of mounted Soldiers induced by IEDs. Physical models, including human cadavers, and frangible and mechanical test devices, are used to develop a better understanding of injury mechanisms in the lower extremities.[3,11–15] Human cadaver models are often accepted as the best representation of the living human leg due to their high level of biofidelity. The drawback of human cadaver models, however, is that there are significant anatomical variations between cadavers, including anthropometry and tissue properties. Furthermore, the age and health status of the cadaver at time of death may not be representative of the Soldier population and it is largely unknown how well the properties of cadaveric tissue represents that of living tissue. Frangible leg models are designed to be representative of an "average" Soldier and eliminate the variation in anthropometry and tissue properties between specimens. However, the material properties are homogeneous and not necessarily accurate simulants of biological tissue. In addition, frangible models generally can only be used once and therefore are not considered cost effective for extensive testing. In contrast, mechanical test devices, such as anthropomorphic test devices (ATDs) can survive multiple tests since they are constructed out of rigid materials. However, the rigidness of the model leads to a different mechanical response than the more compliant human at high rates of acceleration. Thus, the stiff mechanical response of ATDs is not always suitable for studying injury mechanisms of humans in UBB events.

Numerical models are the alternative to the physical models discussed above. The strength of a numerical model is that it can easily be changed to explore the role and importance of a physical effect. These models can simulate a wide range of UBB conditions on the lower extremities and capture the location of where injury initiates and how it propagates. Thus they can evaluate the effectiveness of protection concepts such as energy-absorbing structures. However, as with any numerical tool, numerical models necessarily make assumptions on geometries, boundary conditions, constitutive response, and material parameters.

Numerically modeling the human is a particularly challenging effort requiring careful attention to detail. Numerical models used to study UBB events in the literature have largely been adapted from mature models in the car crash injury, however, this approach may not be appropriate due to the unique loading of UBB events. The large variability in human anthropometry and experimental uncertainty in tissue characterization is largely underrepresented in the simulation literature. In fact, only a small subset of typical material models and their parameters are used to numerically model the human body in UBB events and the anthropometry of the human model is held fixed.

Biological variability, including tissue properties and the anthropometric differences between Soldiers, may play a critical role in injury mechanisms. Numerical understanding of injury mechanisms is simplified by starting with a simpler problem and building physical insight. Here we present a baseline study that only evaluates the role of material parameters on injury mechanisms. The report is organized as follows. Section 2 discusses the details of the model and the boundary conditions of the simulations. Section 3 presents the results of our study including an overview (Section 3.1), a detailed look at 2 illustrative simulations (Section 3.2), the trends of predicted injuries (Section 3.3), the effects of specific parameters on potential injury occurrence (Section 3.4), and the location of predicted failures (Section 3.5). Finally, Section 4 discusses our observations of the results and considers the future direction of the model and its applications.

2. Simulation Details and Injury Prediction

This section describes the anatomical detail captured in our numerical model, the applied loading condition, and our choices in constitutive models. Our method for determining whether a bone would have likely failed due to the applied loading is also discussed.

2.1 Anatomical Details

Figure 1 provides an overview of the simulation geometry, anatomical details, and the loading condition. Initially developed in Kraft et al.,[16] the lower leg model was modified to produce the finite element model used in this work (see Appendix A for additional details). Figure 1a shows the flesh layer (yellow), cortical bone (gray), trabecular bone (orange, see inset) and the steel plate (black) used in the simulations. Thirty bones are explicitly represented, including the femur, patella, tibia, fibula, and the 26 bones of the foot. Both cortical and trabecular bone are modeled in the femur, patella, tibia, fibula, talus, and calcaneus. The bones of the mid- and forefoot are not segmented into different bone types and are assigned cortical bone properties. The soft tissue and skin, also referred to as flesh, is a homogenization of skin, muscles, tendons, connective tissue, blood vessels, etc. using an approach similar to that proposed by Cheung et al.[17] Note that there are more than 100 muscles, tendons, and ligaments in the lower leg that are simplified in taking this assumption. A flesh layer fills in the gaps between the bones and thus details of the joint structures such as cartilage and synovial fluid are not explicitly represented.

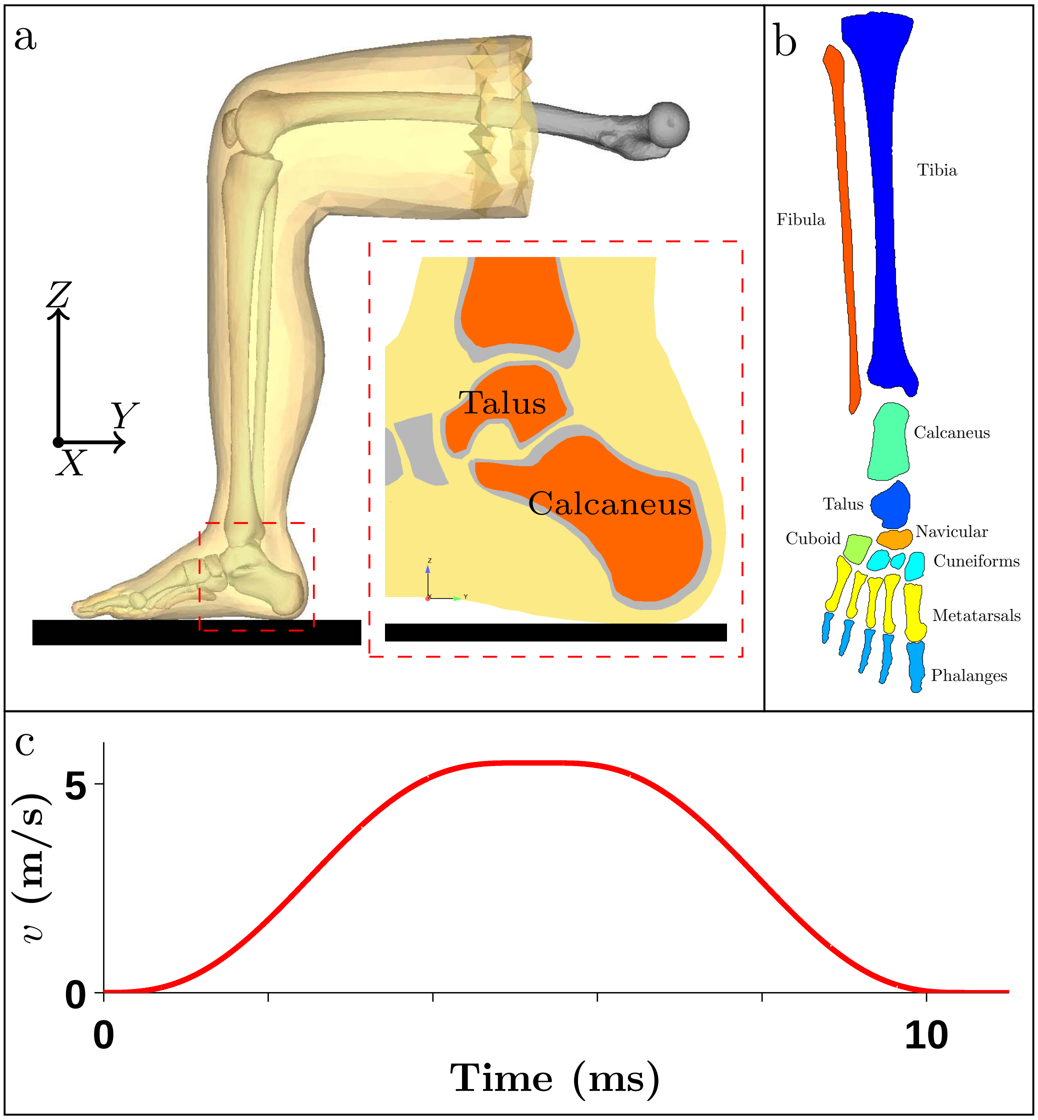

Fig. 1 **Panel *a* provides an overview of the geometry considered in our simulations. The inset in panel *a* (dashed red box) shows a cross-sectional view of the talus and calcaneus where the cortical shell (gray) and trabecular bone (orange) are shown against the flesh (yellow). Panel *b* shows a bone map, a 2-dimensional (2-D) representation of the bones of the lower leg excluding the patella and femur. Labels are provided for all bones. Note that this presentation does not maintain all of the spatial connectivity, e.g., the calcaneus is not in direct contact with the tibia. Panel *c* is a trace of the velocity versus time that is applied to the steel plate in the positive Z-direction.**

The anatomical geometry for the model was obtained from Zygote Media Group, Inc. (American Fork, UT), a company that creates anatomical geometry from CT scans of human specimens who anthropometrically fit within the 50th percentile. The femur and patella were positioned so that the lower leg is in a seated position (90° angles at both the knee and ankle) and initialized so that the foot rests on a steel plate.

2.2 Loading and Boundary Conditions

An idealized velocity history (Fig. 1c) is imposed on the steel plate, which is treated as rigid. This loading condition is similar to those seen in blast events, but is not meant to reproduce a specific threat, merely to capture gross features. Special care is taken to ensure the applied velocity and its derivative are continuous, thus avoiding spurious noise.[18] The mathematical formulation of the smooth curve is described in Appendix B. Initially, the plate is stationary and then over the course of 2 ms is accelerated to a constant velocity of 5.5 m/s before accelerating back to zero. After 10 ms, the plate comes to rest with a displacement of 3 cm. In the first 2 ms, the average acceleration of the plate is 2,750 $\mathrm{m/s^2}$, thus acceleration due to gravity is ignored. The femur is not fixed in any direction.

2.3 Material Details

Extensive testing on bone and soft tissues reveal rate-dependencies and nonlinearities in their constitutive responses. Accurately predicting fracture patterns of bone and subsequent injury requires a rigorous understanding of the constitutive and failure response of the material as well as adequate representations of interfaces and contact surfaces—a resolution that is beyond the current state of the model. To provide a baseline to compare against, we take the rate dependence and nonlinearity of the materials as secondary in importance and assume that the flesh, cortical bone, and trabecular bone behave as isotropic linear elastic materials. As we will discuss in Section 2.4, we use state variables as correlative and predictive of injury but do not attempt to model the actual failure process. We assume that injury occurs from accumulated strain, and thus we treat any rate-dependent failure to be of secondary importance in the problem.

Table 1 is a compilation of constitutive models and their parameters used to represent tissues of the lower leg found within the literature. The first column gives the anatomic component and the second column lists the types of constitutive models used. The third column provides the range of material properties specific to a linear elastic constitutive model that we analyzed in this study. In cases where the constitutive model was not linear elastic, the range is determined by either taking the small strain elastic modulus or an equilibrium modulus. The last column provides the references for the materials. After surveying the literature for a range of material properties used to model tissues in the lower leg, we selected 6 parameters that we varied between relatively low or high values that fell within the ranges reported in the literature. The anatomical components and the material model parameters that we vary are reported in Table 2. For example, in a given simulation the Young's modulus of cortical bone was either 15 or 19 GPa. The density, Young's modulus and Poisson's ratio of trabecular bone, and the bulk modulus and Poisson's ratio of flesh are also varied. Since the flesh is treated as linear elastic, the reporting of its bulk modulus can unambiguously be replaced with a Young's modulus. In all of the simulations the density and Poisson's ratio of cortical bone, as well as the density of flesh, remained fixed. To handle the flesh material parameter values numerically, we utilize a nodal-based tetrahedron,[19] see Appendix A.

Table 1 Compilation of various constitutive models and parameters found in computational models of the lower extremities. Failure stress is given in terms of a von Mises stress criterion.

Anatomic Component	Material Model	Material Properties	References
Trabecular bone	Linear elastic, Elastic-plastic, Transversely isotropic	E = 150–900 MPa ν = 0.3–0.45 ρ = 650–1,100 kg/m^3	[1,20–23]
Cortical bone	Linear elastic, Elastic-plastic, Transversely isotropic	E = 15–19 GPa ν = 0.3–0.35 ρ = 1,680–2,000 kg/m^3 Failure Stress = 124–175 MPa	[1,20–24]
Flesh	Linear elastic, Hyper-elastic, Linear viscoelastic	K = 2.5–300 MPa ν = 0.42–0.49 ρ = 1,000–1,300 kg/m^3	[1,20,21,23]

Note: Not all parameters are listed for each constitutive model. Furthermore, not all lower extremity components are listed. E is the Young's modulus, ν is Poisson's ratio, ρ is density, and K is the bulk modulus.

Table 2 Linear elastic material parameters. Three material parameters were kept constant and 6 material parameters were varied through low or high values to produce 64 combinations.

Anatomic Component	Material Model Parameter	Low Value	High Value	Fixed Value
Cortical bone	ρ	···	···	1,850 kg/m^3
	E	15 GPa	19 GPa	···
	ν	···	···	0.3
Trabecular bone	ρ	650 kg/m^3	1,100 kg/m^3	···
	E	150 MPa	900 MPa	···
	ν	0.3	0.45	···
Flesh	ρ	···	···	1,000 kg/m^3
	K	20 MPa	300 MPa	···
	ν	0.42	0.48	···

Note: E denotes Young's modulus, ν denotes Poisson's ratio, ρ is density, and K is the bulk modulus.

2.4 Correlating State Variables to Injury Prediction

Injury can occur over multiple length scales and involve cellular processes as well as the mechanical disruption of tissue. The numerical simulations solve for the mechanics of the problem, but correlating a state variable or variables with injury is an ongoing field of research. Typically, principal stress or strain, peak stress or strain, pressure, and von Mises stress are used as the criteria to trigger failure in finite element models through element deletion, degradation of the elastic modulus, or cohesive failure in elements. However, once failure occurs, these numerical simulations typically diverge from what is seen experimentally, as fracture is a difficult phenomenon to model. Accurately predicting the particular injury of bone fracture requires a detailed understanding of material properties as well as the microstructure of the tissue. Since the spatial resolution of our model is insufficient to predict precise fracture patterns, our focus is whether certain bones would likely have fractured during an event. These simulations establish trends of how particular combinations of material parameters affect the observed stresses.

We assume that a mechanical state variable such as pressure or von Mises stress can be used as an injury predictor, i.e., a correlative measure for a condition that would ultimately result in injury. We are using the convention that normal stresses are negative in compression and define pressure as negative one-third the trace of the Cauchy stress. We restrict ourselves to stresses observed in the cortical shell bone. The constitutive model we use to represent the cortical tissue is isotropic linear elastic and implies that strain and stress can be interchanged uniquely. The specific choice of an injury predictor is an open research endeavor. As one might imagine, the reduction of the time history of a symmetric rank-3 tensor to an injury predictor is extremely open ended and material specific. Without experimental measurements to conclusively reveal a predictor, we use von Mises stress and pressure since they are both reduced representations of the complete stress state and are scalar valued. The von Mises stress is a typical indicator of failure in other materials and the ranges in Table 1 correspond to the elastic-plastic failure values used for cortical bone. Pressure, on the other hand, is not commonly used as an indicator of injury in simulations. However, it also represents a directionally free and potentially physically meaningful choice.

Other common choices for injury predictors include “axial stress”, principal stresses, and the maximum of the principal stresses. The complicated geometry, especially at interfaces, makes axial stress not universal to the entire bone geometry. Similarly, the ambiguity in using the principal stresses arises from a complicated geometry and stress state, i.e., there is little-to-no meaning of the eigenvectors from element to element or from time to time making their values difficult to interpret. The notion of the maximum of the eigenvalues of ever changing directions also carries little practical meaning. If a microstructural detail was known, however, and included within the model, e.g., osteon direction, the stress oriented with this microstructural detail might be an extremely useful injury predictor.

The approach we take to predicting injury is as follows. The completed simulation is postprocessed to determine whether any elements within the cortical shell exceed an injury predictor threshold. The 2 injury predictors we consider are von Mises stress and magnitude of pressure. We select a wide range of threshold values so that we can assess any sensitivity of predicted injury on the specific choice of threshold. For the von Mises stress injury predictor we consider the range of failure reported in Table 1. Since it is not typically used in the literature, the range of interest was widened for the pressure predictor. The interpretation of the data needs to be carefully considered since the transmission of stress through bone will change between fractured and unfractured cases.

Postprocessing was performed using GROPE and ALGEBRA (SEACAS Toolkit, Sandia National Laboratory), and MATLAB. Using GROPE and ALGEBRA, elements can be probed using text commands following the completion of a simulation. Additionally calculations can be made quite rapidly, including picking the maximum value over time. These tools were used to determine the pressure and von Mises stress over time (for each microsecond) for all elements.

3. Results

Six material parameters of the cortical bone, trabecular bone, and flesh were varied between low and high values, producing 64 combinations of material properties. The specific values of material properties are reported in Table 3. Each of these simulations can be thought of as a proxy for a Soldier with a slightly different tissue characterization, all within the accepted range of values shown in Table 1. The results are organized as follows. Section 3.1 provides an overview of the simulations. Section 3.2, considers 2 simulations in detail. Section 3.3, comments on the trends of the injury predictor found across the data sets. Section 3.4 reports on the occurrence of failure based on the material parameters themselves. Finally, we report on the localization of stress in Section 3.5.

Table 3 Material properties of 64 simulations produced by varying 6 material parameters

#	E_{cort} (GPa)	ρ_{trab} (kg/m^3)	E_{trab} (GPa)	ν_{trab}	K_{Flesh} (MPa)	ν_{Flesh}	#	E_{cort} (GPa)	ρ_{trab} (kg/m^3)	E_{trab} (GPa)	ν_{trab}	K_{Flesh} (MPa)	ν_{Flesh}
1	15	650	0.15	0.3	20	0.42	33	19	650	0.15	0.3	20	0.42
2 ✓	15	650	0.15	0.3	20	0.48	34	19	650	0.15	0.3	20	0.48
3	15	650	0.15	0.3	300	0.42	35	19	650	0.15	0.3	300	0.42
4	15	650	0.15	0.3	300	0.48	36	19	650	0.15	0.3	300	0.48
5	15	650	0.15	0.45	20	0.42	37	19	650	0.15	0.45	20	0.42
6	15	650	0.15	0.45	20	0.48	38	19	650	0.15	0.45	20	0.48
7	15	650	0.15	0.45	300	0.42	39	19	650	0.15	0.45	300	0.42
8	15	650	0.15	0.45	300	0.48	40	19	650	0.15	0.45	300	0.48
9	15	1100	0.15	0.3	20	0.42	41	19	1100	0.15	0.3	20	0.42
10	15	1100	0.15	0.3	20	0.48	42	19	1100	0.15	0.3	20	0.48
11	15	1100	0.15	0.3	300	0.42	43	19	1100	0.15	0.3	300	0.42
12	15	1100	0.15	0.3	300	0.48	44	19	1100	0.15	0.3	300	0.48
13	15	1100	0.15	0.45	20	0.42	45	19	1100	0.15	0.45	20	0.42
14	15	1100	0.15	0.45	20	0.48	46	19	1100	0.15	0.45	20	0.48
15	15	1100	0.15	0.45	300	0.42	47	19	1100	0.15	0.45	300	0.42
16	15	1100	0.15	0.45	300	0.48	48 ✓	19	1100	0.15	0.45	300	0.48
17	15	650	0.90	0.3	20	0.42	49 ✓	19	650	0.90	0.3	20	0.42
18	15	650	0.90	0.3	20	0.48	50 ✓	19	650	0.90	0.3	20	0.48
19	15	650	0.90	0.3	300	0.42	51 ✓	19	650	0.90	0.3	300	0.42
20	15	650	0.90	0.3	300	0.48	52	19	650	0.90	0.3	300	0.48
21	15	650	0.90	0.45	20	0.42	53	19	650	0.90	0.45	20	0.42
22	15	650	0.90	0.45	20	0.48	54 ✓	19	650	0.90	0.45	20	0.48
23	15	650	0.90	0.45	300	0.42	55	19	650	0.90	0.45	300	0.42
24	15	650	0.90	0.45	300	0.48	56 ✓	19	650	0.90	0.45	300	0.48
25	15	1100	0.90	0.3	20	0.42	57	19	1100	0.90	0.3	20	0.42
26	15	1100	0.90	0.3	20	0.48	58	19	1100	0.90	0.3	20	0.48
27	15	1100	0.90	0.3	300	0.42	59	19	1100	0.90	0.3	300	0.42
28	15	1100	0.90	0.3	300	0.48	60	19	1100	0.90	0.3	300	0.48
29	15	1100	0.90	0.45	20	0.42	61	19	1100	0.90	0.45	20	0.42
30	15	1100	0.90	0.45	20	0.48	62 ✓	19	1100	0.90	0.45	20	0.48
31	15	1100	0.90	0.45	300	0.42	63	19	1100	0.90	0.45	300	0.42
32	15	1100	0.90	0.45	300	0.48	64 ✓	19	1100	0.90	0.45	300	0.48

Note: A check mark indicates that the simulation terminated early, i.e., before 3.5 ms. Blue rows indicate the 2 illustrative simulations discussed in Section 3.2. The 4 green rows isolate a specific subset where flesh properties are varied and are discussed in Section 3.3. The 7 orange rows are a subset where predicted injuries followed a different trend discussed in Section 3.3.

3.1 Summary of Simulations

In total, 64 simulations were executed for all the combinations of material parameters discussed in Section 2. These simulations are enumerated as rows in Table 3. Each column entry in Table 3 gives the value of a material parameter used in that particular simulation. As described in Section 2.2, every simulation experiences the same loading condition. Cauchy stress tensor data was output for all elements every 0.1 μs (simulation time). Each simulation used 128 cores and was allowed a walltime of 48 hours. Typically, this walltime was sufficiently long enough for a simulation to reach 17 ms (simulation time) and output 400 GB of raw data per simulation. Regular hard drive write commands slowed the performance of the solver. Of the 64 simulations, 55 of them reached or exceeded 3.5 ms of simulation time before either terminating from a negative volume or running out of walltime due to a plummeting time step. Simulations that failed before 3.5 ms are denoted in Table 3 by a checkmark under the column labeled ET. Thirteen rows in Table 3 are highlighted blue, green or orange. The blue rows are 2 illustrative simulations (Simulations 1 and 3) that have been separated out and studied in more detail in Section 3.2. The 4 green rows (Simulations 9 through 12) and the 7 orange rows (Simulations 18, 22, 26, 30, 50, 54, and 58) are discussed in Section 3.3.

The 55 simulations that reached or exceeded 3.5 ms represent roughly 86% of the total simulations. By 3.5 ms, the plate is displaced 6 mm and reaches a velocity of 4.6 m/s, which is 84% of the 5.5 m/s maximal value of the velocity loading seen in Fig. 1c. Only 26 simulations (40%) reached or exceeded 5 ms of simulation time. The plate in these simulations reaches maximal velocity and has the largest displacements ($\geq$14 mm). Of the 9 simulations that terminated before 3 ms of simulation time (denoted by a check mark in Table 3), 7 of them had a similar set of material properties. These include a cortical Young's modulus of 19 GPa and a trabecular Young's modulus of 900 MPa. Five of the 9 simulations that terminated early had a cortical Young's modulus of 19 GPa, a trabecular Young's modulus of 900 MPa, and a trabecular density of 650 kg/m^3. Seven of the 9 simulations that terminated early had the higher Poisson's ratio for the soft tissue of 0.48. It is unclear whether these parameter combinations are significant for numerical stability. However, none of the simulations with the low soft tissue bulk modulus exceeded 5 ms of simulation time.

3.2 Two Illustrative Cases

This section considers 2 simulations in detail. The only difference in material parameters is the bulk modulus of the flesh. The material properties corresponding to these simulations are highlighted in blue in Table 3, where Simulation 1 had the low soft tissue bulk modulus value (20 MPa) and Simulation 3 had the high soft tissue bulk modulus value (300 MPa). The remaining material properties in these simulations were assigned low values. We first present time history results and then consider the injury prediction capabilities of these simulations, i.e., the sensitivity and susceptibility of specific bones to failure.

Figures 2 and 3, respectively, show the time histories of the pressure and von Mises stress localization in the deformed configuration. The 2 perspectives were chosen to highlight some of the structurally important regions of the calcaneus and talus. Each row corresponds to a different time indicated at the far left side of the figure. The results from Simulation 1 (low bulk modulus) are presented in the left column and the results from Simulation 3 (high bulk modulus) are presented in the right column. Note that the maximum values on the color scales are quite different for Figs. 2 and 3, i.e., different magnitudes were seen when comparing von Mises stress and pressure.

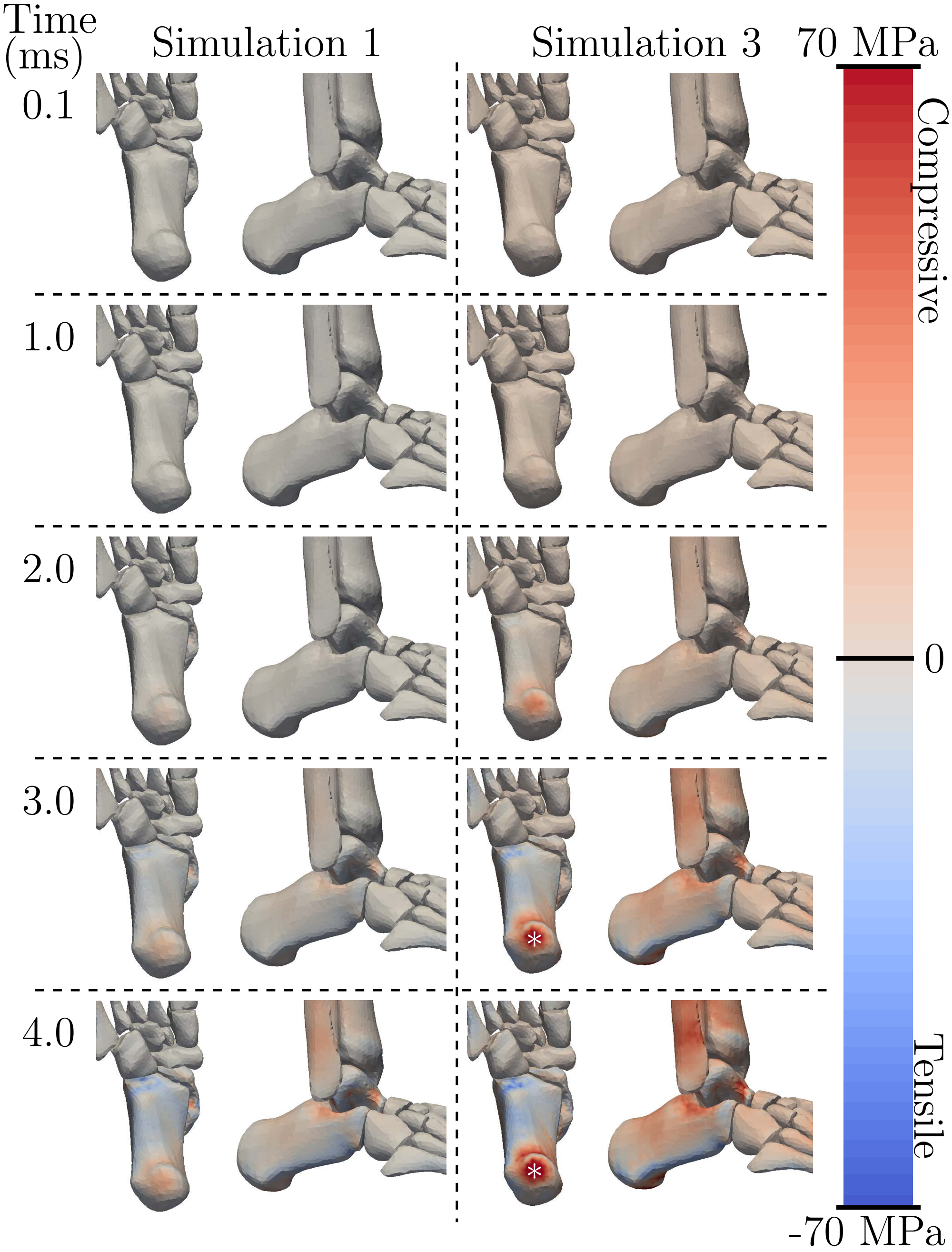

Fig. 2 **Pressure localization throughout time for Simulation 1 and Simulation 3. Two different views of the model are presented for each simulation. The time of the simulation is indicated at the far left side of the figure and applies to both simulations. The $*$ in the figure indicates locations that exceed the color scale.**

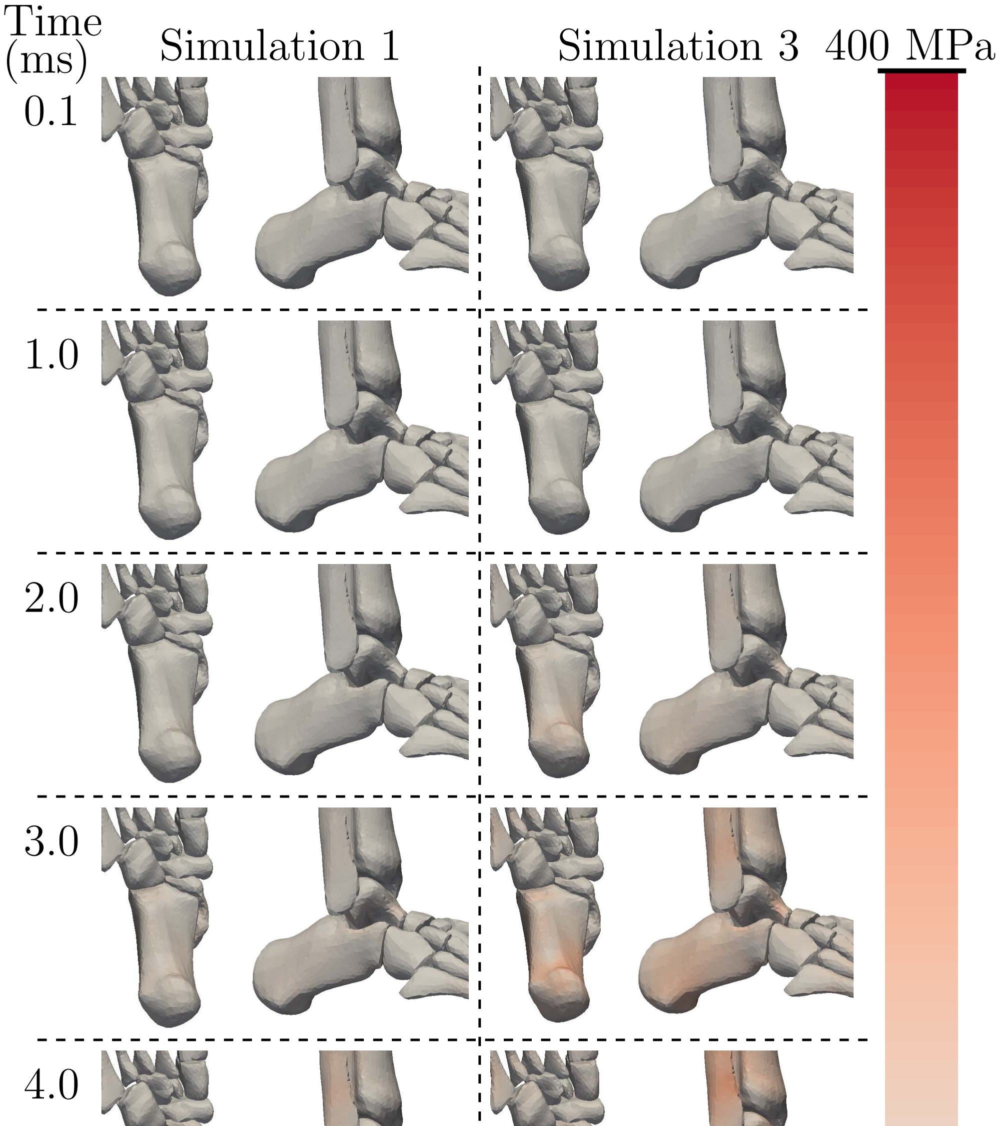

Fig. 3 von Mises stress localization throughout time for Simulation 1 and Simulation 3. Two different views of the model are presented for each simulation. The time of the simulation is indicated at the far left side of the figure and applies to both simulations.

The time history results for pressure are qualitatively similar between simulations. As time progresses, the magnitude of pressure increases and the stress states are similar between simulations, i.e., compressive regions and tensile regions appear in similar anatomical locations. As one looks at the false color throughout time, the color patterns only increase in intensity as opposed to changing in color. In both simulations, compressive pressures are seen at the interface between the calcaneus and talus, and the pressure is largely tensile on the inferior surface of the calcaneus (on what would be considered the “under side” of the calcaneus) nearest the cuboid and cuneiforms. In addition to the similarities between the 2 calcanei, there are similarities in the pressure distribution for the fibula and talus as well. The fibula experiences compressive pressure just above the ankle joint (lateral malleolus). The talus experiences compressive pressure where it meets the calcaneus and cuneiforms. There are similarities in the stress localization when considering the von Mises stress as well. Figure 3 shows that the calcaneus again experiences large stresses on its inferior surface. Furthermore, there is some localization of the shear stresses in the fibula.

Quantitatively, however, the 2 simulations are quite different. At 0.1 ms, the pressures in Simulation 3 can be seen as a light pink (Fig. 2). In Simulation 1, these pressures are not readily visible until the 2.0 ms panel. Four milliseconds into Simulation 3, the portion of the calcaneus nearest the steel plate (calcaneal tuberosity) experiences compressive pressures that exceed the color scale, whereas in Simulation 1 they are significantly smaller. Similar observations can be made when comparing the color intensity values in Fig. 3.

Single element time histories of the pressure and von Mises stress from the cortical shell of 6 bones are presented in Fig. 4. Each color corresponds to a different bone and the relative location of each element is indicated with a circle in panel *a*. An open circle indicates that the element is on the side of the bone not visible from the current view point. Pressure results from Simulations 1 and 3 are plotted in panels *b* and *c*, respectively, and von Mises stress results are shown in panels *d* and *e*. The inset in panels *b*–*e* show the early time (less than 1 ms) behavior of those same points. The vertical dashed lines in panels *b* and *d* indicate the time at which Simulation 1 terminated.

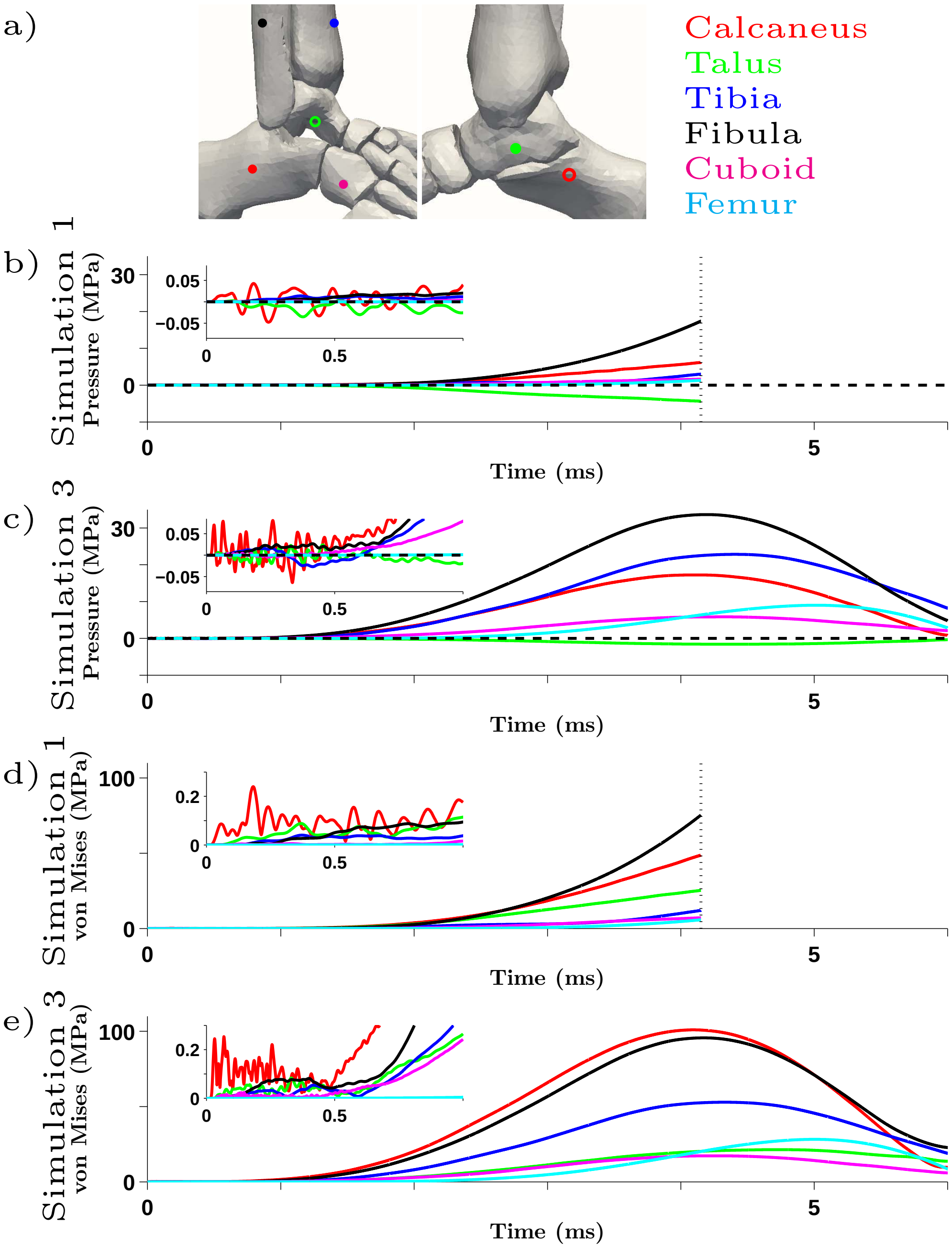

Fig. 4 Time histories for the pressure and von Mises stress from selected elements in the cortical layer of various bones. Each color corresponds to an element in a particular bone. Pressure results from Simulations 1 and 3 are plotted in panels *b* and *c* and von Mises stress in panels *d* and *e*. The inset in each figure shows the early time behavior.

Simulation 3 provides a clear overview of the result of the loading on the lower leg. Panel *c* presents the pressure histories throughout time. For early times, i.e., times less than 1 ms, the elements oscillate between compressive and tensile states (see inset). This is most notable in the calcaneus (red trace). During this initial transient state, the amplitude of the oscillations are small with values less than 0.5% of the peak values observed in the plot. For times greater than 1 ms, the transient oscillatory behavior gives way to a smooth accumulation of pressure followed by a smooth reduction of pressure. The largest peak pressure occurs in the fibula (black trace, panel *c*), which reaches a maximum value of approximately 30 MPa around 4.2 ms. This is followed by the tibia (blue trace) with a pressure of approximately 20 MPa around 4.3 ms and the calcaneus (red trace) with a pressure of 15 MPa at 4.1 ms. During the times presented, the element in the talus is the only one to experience a tensile (negative) pressure. Qualitatively similar observations can be made for the von Mises stresses in Simulation 3 (panel *e*). During the initial transient period, there are high-frequency oscillations in von Mises stress of the calcaneus. The elements from the other bones, however, exhibit fewer oscillations. The initial transient period gives way to a smooth accumulation of stress that rises to a peak value and then falls. The von Mises stress peaks largest in the calcaneus at 100 MPa around 4.1 ms, followed by the fibula at 90 MPa at approximately the same time.

The early time behavior for the pressure (panel *b*, inset) in Simulation 1 is also oscillatory in nature and small in amplitude. However, comparing the calcaneus traces between the 2 simulations reveals higher frequency content present in the signal for Simulation 3, the high case for the bulk modulus of the flesh. The differences in these 2 oscillations is likely due to ringing occurring in the soft tissue of the heel pad between the calcaneus and the steel plate.

After the initial transient period, both the pressure and von Mises stress in Simulation 1 increase smoothly up to the point at which the simulation terminates. Although impossible to verify, based on the nature of the loading, one might assume that the qualitative features of Simulation 1 would be similar to Simulation 3. We can, however, compare the peak values between panels *b* and *c* or stress in panels *d* and *e*. In Simulation 3, the pressure in the fibula (black trace, panel *c*) reaches a maximum value of approximately 30 MPa around 4.1 ms. Around this same time, the fibula in Simulation 1 (black trace, panel *b*), has a pressure of about 15 MPa. A similar observation can be made by comparing the fibula probe in panels *d* and *e*, however, in this case Simulation 1 reaches approximately 70% of the peak value experienced in Simulation 3.

At 4.1 ms it is clear that the distribution of stress is different between the 2 simulations. For instance, compare the order of colored traces from largest to smallest in panels *d* and *e*. In Simulation 1 (panel *d*) the order from largest stress to smallest is the probe in the fibula, calcaneus, talus, tibia, cuboid, and femur. In Simulation 3 (panel *d*) the order is calcaneus, fibula, tibia, femur, talus, and cuboid. These are results from single element probes but whose values strongly depend on the value of the bulk modulus of the flesh.

After the initial transient period, the time histories presented in Fig. 4 show a clear maximum value for both pressure and von Mises stress. Thus, we reduce the data further by considering peak values of pressure and von Mises stress, which we present in a 2-D schematic of the lower leg or *bone map* (Figs. 5 and 6). These figures allow a quick assessment of a particular bone's sensitivity to reaching injurious pressures or von Mises stress levels during a simulation and thus can be used to assess trends in predicted injury.

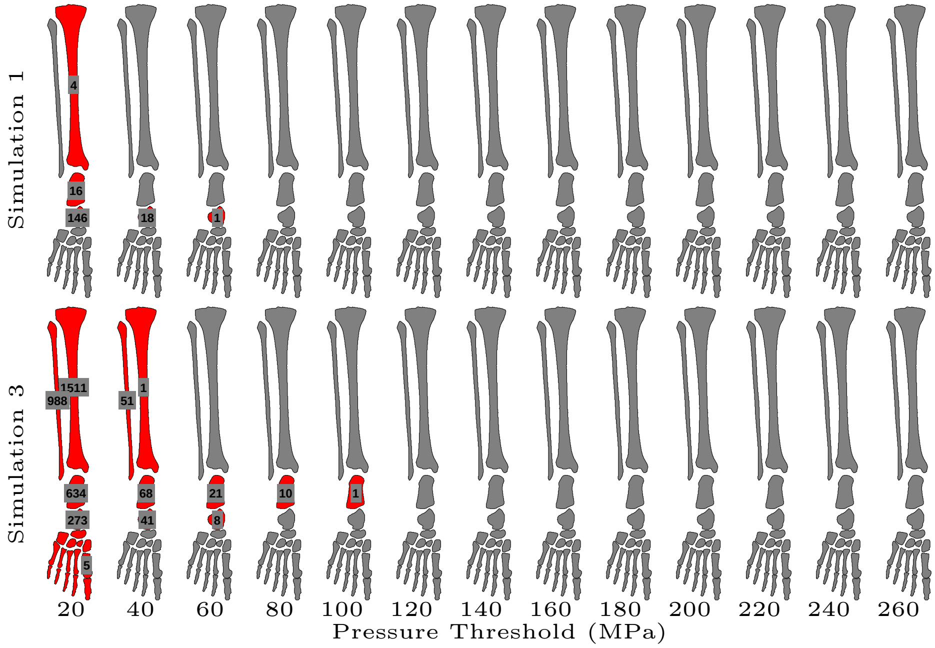

Fig. 5 Bone maps using the pressure magnitude criteria for Simulations 1 and 3 (highlighted in blue in Table 3)

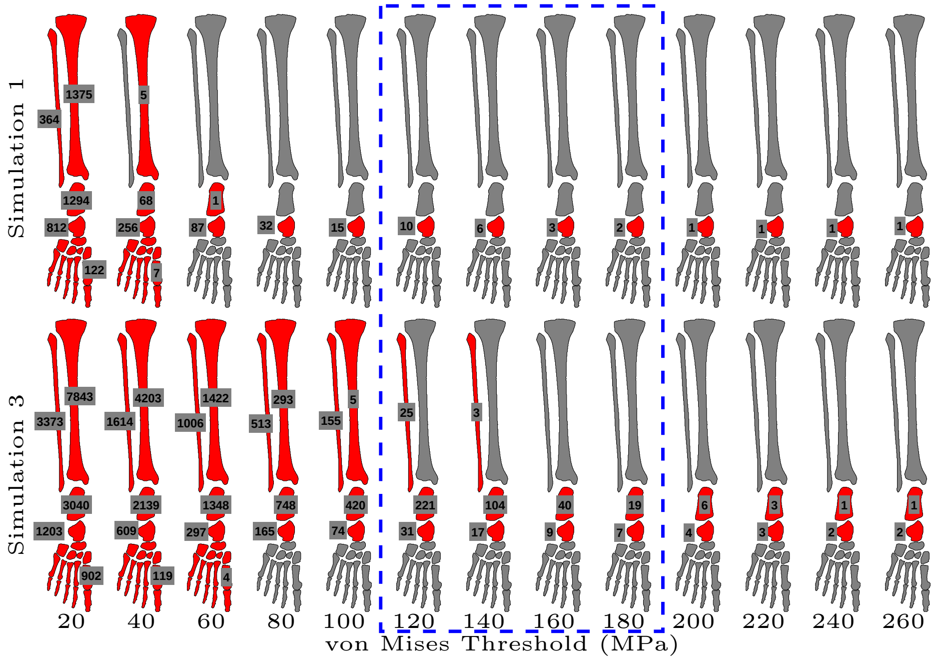

Fig. 6 Bone maps using the von Mises criteria for Simulations 1 and 3 (highlighted in blue in Table 3). The blue dashed box represents the failure range as considered in the current study.

Figures 5 and 6 compare the pressure or von Mises injury predictor for Simulation 1 and Simulation 3, respectively. Each column of the figure corresponds to a particular threshold level. A bone that is colored red indicates that at least one element in the cortical layer of that bone exceeded the threshold, whereas a gray bone signifies that no elements of that bone exceeded the threshold. If a bone has been highlighted red, the number of elements that exceeded the threshold is noted on or near the bone. The numbers provide some insight into the significance of the color coding, i.e., if only a single element exceeds the threshold it is unlikely to be a strong indicator. The bones of the forefoot are grouped as one bone for this analysis. A naming key for the bones can be found in Fig. 1b.

Figure 5 presents the pressure criteria used for predicting injuries. Similar to the observations made in Fig. 4, the stresses in Simulation 3 were typically larger than those in Simulation 1. The first column shows that the tibia, calcaneus, and talus in Simulation 1 experience pressure larger in magnitude than 20 MPa. The second and third columns show that only the talus meets the noted threshold. The number of elements that exceed the thresholds in these cases are most significant for the talus and calcaneus. In contrast, the first column for Simulation 3 shows that each bone has at least one element that exceeds 20 MPa of pressure. The numbers of elements in this case are significant for all of the bones except the forefoot. The 2 bones that experience the largest pressures in Simulation 3 are the calcaneus, which exceeds 100 MPa, and the talus, which exceeds 60 MPa.

Figure 6 presents the von Mises injury predictor for Simulation 1 and 3. In contrast to Fig. 5, the magnitude of stress in Fig. 6 is much larger. The range of failure thresholds used in the literature and summarized in Table 1 is indicated in Fig. 6 by the dashed blue rectangle. The von Mises injury predictor for Simulation 1 shows that the talus exceeds a von Mises stress of 260 MPa, but that no other bones exceed 80 MPa. Simulation 3, in contrast, shows that both the calcaneus and talus exceed 260 MPa, the largest threshold exceeded by the fibula was 140 MPa, followed by the tibia, which reaches 100 MPa. Recall that the only difference between Simulation 1 and Simulation 3 was the value of the bulk modulus for the flesh. For these 2 simulations, the higher soft tissue bulk modulus led to larger stresses in the cortical shells of the bones within the observation time frame.

3.3 Trends in Predictive Injury

Here we present the trends observed after reducing the data sets to their respective bone maps. Eleven specific simulations are also discussed, which are highlighted in either green or orange in Table 3.

After surveying both the von Mises and the pressure injury predictor bone maps for all of the simulations, we made the following observations. Using either injury predictor, the most commonly injured bones were the talus and calcaneus. For a fixed failure threshold, very few injuries were predicted in the forefoot compared to the other bones. It was common to see both the talus and the calcaneus share the same injury prediction sensitivity, but there were some interesting deviations from this trend. In some cases, the calcaneus and talus were so susceptible to injury that even the largest von Mises threshold of 260 MPa was exceeded. This is seen in Simulations 3, 7, 11, 15, 35, 39, 43, and 47, which all ran with the higher flesh bulk modulus and the lower trabecular bone Young's modulus value. The only cases where the calcaneus was more susceptible to injury than the talus were cases where we analyzed the pressure. This occurred for Simulations 3, 7, 8, 11, 15, 16, 35, 36, 39, 40, 43, 44, 47, and 48, which is essentially the same set of simulations as the group where the calcaneus and talus exceeded the 260 MPa von Mises threshold.

In Simulations 9–12, only the Poisson's ratio or bulk modulus of flesh was varied (green rows, Table 3). In these simulations, the properties for cortical and trabecular bone were assigned the same low or high value. The von Mises injury predictor and pressure injury predictor bone maps are presented in Figs. 7 and 8, respectively. For each figure, a row corresponds to a different simulation.

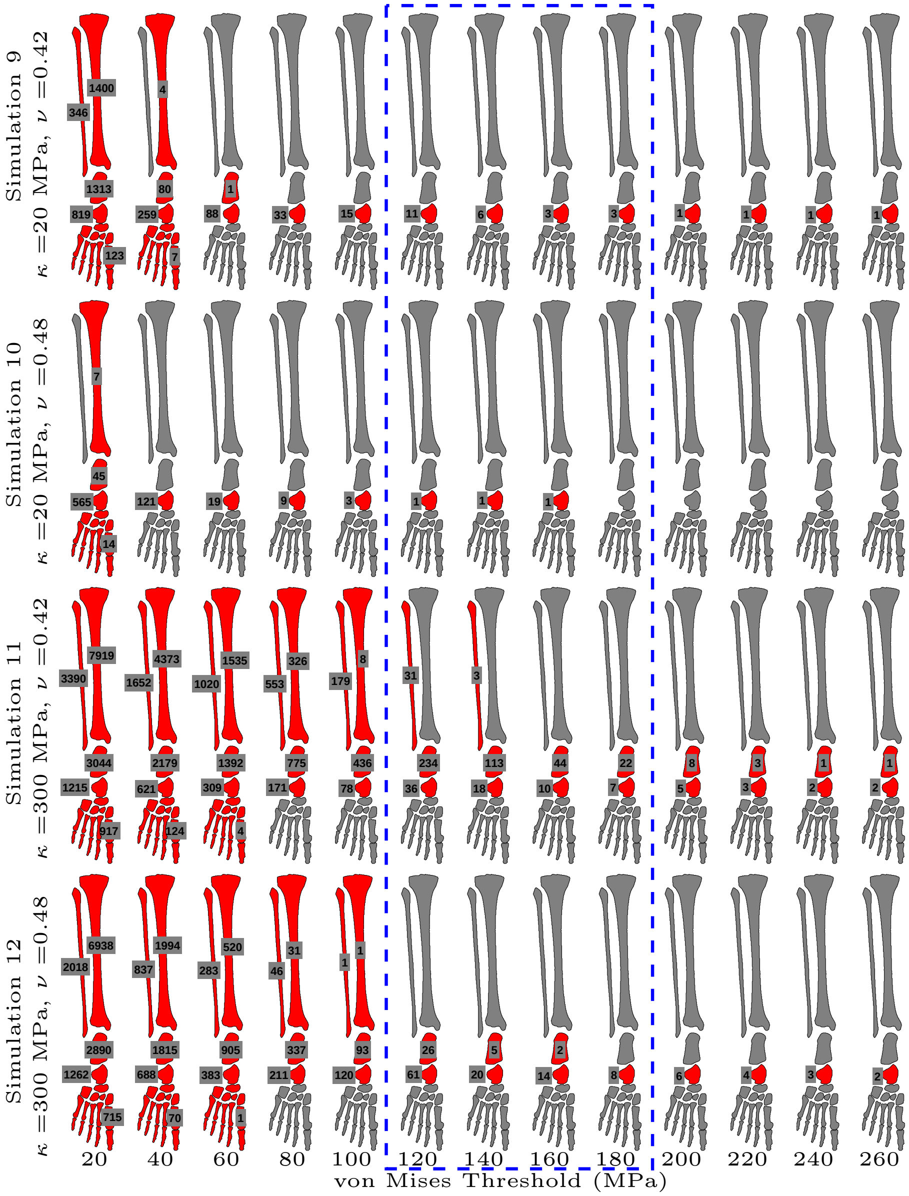

Fig. 7 Bone maps using the von Mises threshold criteria for Simulations 9–12 (highlighted green in Table 3). The blue dashed box represents the failure range as considered in the current study.

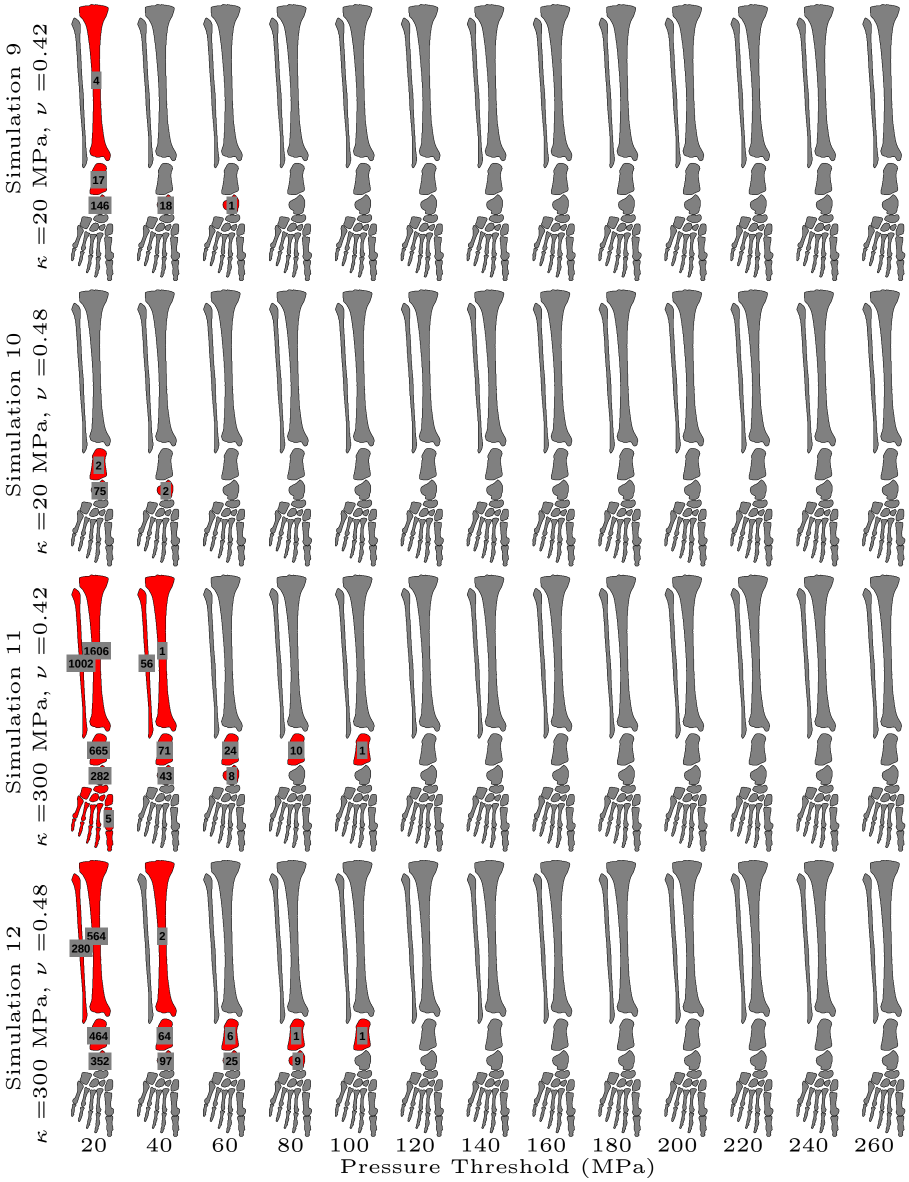

Fig. 8 Bone maps using the pressure threshold criteria for Simulations 9–12 (highlighted green in Table 3)

Figure 7 considers the sensitivity to bone failure for the 4 simulations as it depends on the von Mises stress injury predictor. The only difference between Simulations 9 and 10, and Simulations 11 and 12 is the value of Poisson's ratio. Based on the number of elements that have reached a threshold criteria in the highlighted bones (red), we predict that Poisson's ratio had little effect on the amount of damage we see in the bones. The parameter that has a larger role in the number of injured bones is the bulk modulus of flesh. This observation is made by comparing Simulations 9 and 10, which were run with the lower bulk modulus value, against Simulations 11 and 12, which were run with the higher value. Consider, for example, a single von Mises stress threshold of 140 MPa. In Simulation 9, there are 6 elements in the talus that meet this criteria, and for Simulation 10 there is only one. In contrast, the talus in Simulations 11 and 12 had 18 and 20 elements, respectively, that met the criteria. Simulation 11 also showed that 3 elements in the fibula and 113 elements in the calcaneus reached the injury threshold, and Simulation 12 showed that 5 elements in the calcaneus reached this same injury threshold.

By considering a single bone and varying the threshold, we also get an intuitive picture of the sensitivity of injury prediction for that particular bone. The talus in Simulations 9, 11, and 12 predicts injury regardless of the threshold, thus making it virtually insensitive to our injury predictor. This was a common trend observed seen for the talus. In contrast, predicting injury in the calcaneus is sensitive both to the threshold of the injury predictor as well as the material properties used in the simulations.

Figure 8 presents the predicted injuries for Simulations 9 through 12 using the pressure injury criteria. Save for the lowest injury threshold of 20 MPa in Simulation 11, the forefoot region does not show any elements above threshold for injury prediction and is therefore virtually insensitive to the pressure injury criteria in these 4 simulations. The other bones, however, do show some sensitivity, although for much lower thresholds than the von Mises criteria. The most interesting feature that comes from analyzing the pressure injury predictor is seen by comparing Simulations 9 and 10 with Simulations 11 and 12. Recall that using the von Mises stress injury predictor, the talus was virtually insensitive to the threshold value and typically predicted failure. Using the pressure injury predictor we begin to see cases where the talus is no longer overly sensitive to predicting injury. By comparing the talus and the calcaneus in Simulations 9 and 10, one can see that the talus experiences larger pressures than the calcaneus. However, this trend is reversed for Simulations 11 and 12 where the calcaneus experiences larger pressures than the talus. This feature is important since it implies that a pressure injury criteria failure threshold can be picked such that the calcaneus will predict failure *without* the talus predicting failure as well.

We conclude the discussion of the bone map results by considering Simulations 18, 22, 26, 30, 50, 54, and 58, the orange rows in Table 3. These are cases where the talus was extremely susceptible to pressure predicted injury, but the calcaneus was not, i.e., the talus was always above threshold and the calcaneus was rarely predicted as injured. Of these 7 simulations, 5 reached simulation times of 3.5 ms but did not greatly exceed 3.5 ms, and the remaining 2 only reached 3.1 ms. All 7 simulations had the same trabecular Young's modulus of 900 MPa, soft tissue properties of bulk modulus 20 MPa, and Poisson's ratio of 0.48.

3.4 Distribution of Predicted Injury

Here we survey the occurrence of predicted injuries specific to individual bones. As reported in Section 3.1, the talus and calcaneus were common locations of injury. The histograms in Figs. 9 and 10 report the general effect of a material parameter on predicted injury. Failure occurrence is reported for the calcaneus, talus, tibia, fibula and forefoot based on the value used for that material parameter (Figs. 9, 10, and Appendix C). Failure is said to occur during a simulation for a particular bone if at least one element in the cortical shell exceeds the injury predictor threshold. Both von Mises stress and pressure injury predictors were considered. These histograms were created for each of the 6 material parameters, and the 2 failure criteria.

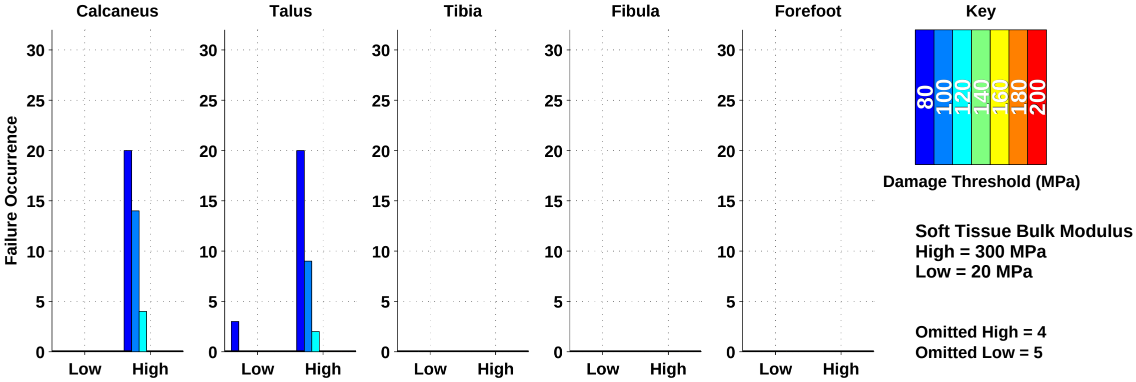

Fig. 9 Failure occurrence in each bone varying the bulk modulus of flesh using a pressure injury predictor. Failure occurrences are tallied at various bones for a range of thresholds. Each panel is specific to an individual bone and tallies the number of simulations for which the absolute value of the pressure within any element in the bone exceeded the damage threshold. The bar colors indicate which damage threshold the tally corresponds to. Low and high values for the material parameter as well as the specific damage thresholds used are indicated on the right under the key.

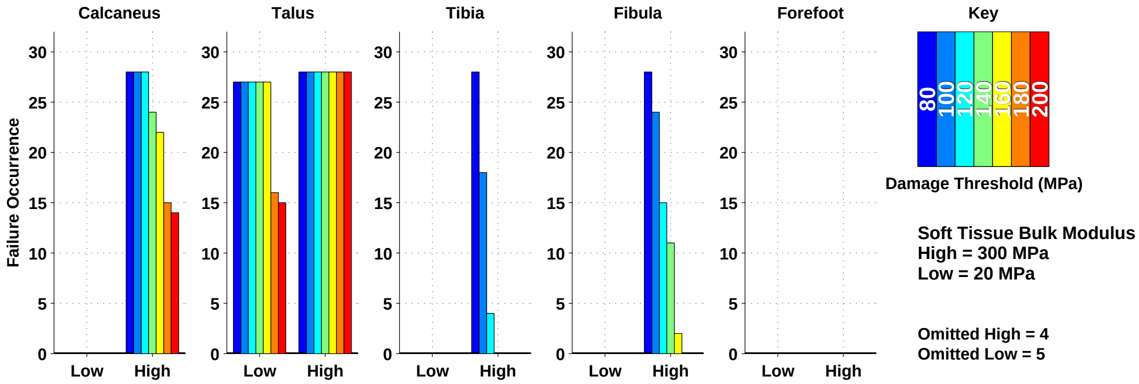

Fig. 10 Failure occurrence in each bone varying the bulk modulus of flesh using a von Mises stress injury predictor. Failure occurrences are tallied at various bones for a range of thresholds. Each panel is specific to an individual bone and tallies the number of simulations for which the von Mises stress within any element in the bone exceeded the damage threshold. The bar colors indicate which damage threshold the tally corresponds to. Low and high values for the material parameter as well as the specific damage thresholds used are indicated on the right under the key.

Figure 9 divides the simulations by their soft tissue bulk modulus and considering the results from using the pressure injury predictor. Histograms are shown for the calcaneus, talus, tibia, fibula, and forefoot. Failure occurrence refers to a maximum of 32 simulations, in either the low or high category. Seven threshold values were considered to investigate the sensitivity of failure. These 7 values include and extend beyond the range listed in Table 1. The value of the threshold is indicated by the color of the bar in the key. The key also contains the number of simulations that did not reach 3.5 ms and therefore were omitted from the histogram. Consider, for example, the panel dedicated to the calcaneus in Fig. 9. The tall, dark blue bar that reaches the number 20 indicates that 20 out of the 32 simulations that were run with a high flesh bulk modulus had at least one element exceed the pressure damage threshold of 80 MPa. Similarly, Fig. 10 looks at the effect of the flesh bulk modulus on von Mises failure. Figures C-1 through C-10 in Appendix C explore the same question for the other 5 material parameters that were varied in the study.

The material property that had the strongest influence on occurrences of predicted injury was the bulk modulus of the flesh. This effect is most clearly demonstrated in Fig. 10. By considering the panel dedicated to the calcaneus, one can see that, when using the high bulk modulus value of 300 MPa, a significant number of simulations predicted calcaneus failures across the different damage thresholds (e.g., 28 simulations out of 32 for a threshold value of 120 MPa). There is also a high occurrence of predicted injury in the tibia and fibula in the high bulk modulus cases. In contrast, the low bulk modulus cases do not predict any injuries in the calcaneus, tibia, or fibula. The Poisson's ratio of the soft tissue and the Young's modulus of cortical and trabecular bone exhibit a minor effect on predicted injury. There was no clear trend of predicted injury on the density or Poisson's ratio of trabecular bone. Note that none of the low cases for the soft tissue bulk modulus exceed a simulation time of 5 ms.

3.5 Stress Localization

Sections 3.1 and 3.4 reported that injuries to the calcaneus and talus were common amongst the simulations. While the histograms presented in Section 3.4 show the number of simulations with these injuries, the specific element location is not reported. Here we consider the localization of the largest stresses of the problem.

Each panel in Fig. 11 presents the calcaneus from 1 of 6 different orthogonal views. The calcaneus has been colored dark gray with additional colors superimposed on top of it. The color indicates whether that specific element in at least 1 of the 64 simulations exceeded a specific threshold, thus blocks of uniform color indicate multiple elements from multiple simulations all meeting the same criteria. In each panel, the color red indicates pressures larger than 80 MPa, blue represents pressures less than –80 MPa, and green signifies von Mises stress exceeding 150 MPa. These 3 colors are treated as additive so that the appearance of yellow in the panel means that both the green and red conditions have been meet. Cyan illustrates that the blue and green conditions have been met, and black indicates all 3 conditions have been met. An additive of red and blue, i.e., both pressure extremes without a von Mises extreme was not observed. The large red patch at the calcaneal tuberosity, most visible in panels *d, e,* and *f* reveals a patch of elements experiencing large compressive pressures. This observation was also made specifically for Simulations 1 and 3, when discussing Fig. 2. This patch of elements are on the portion of the calcaneus closest to the steel plate. The large green patch, most visible in panels *a* and *e* corresponds to a region of large von Mises stress concentration along the medial side of the calcaneus. The last notable collection of elements are multicolored and can be seen in panel *e*, a view through the phalanges to the calcaneus. Both large von Mises stresses and tensile pressures are observed on the inferior surface of the calcaneus, the point on the calcaneus nearest the talus.

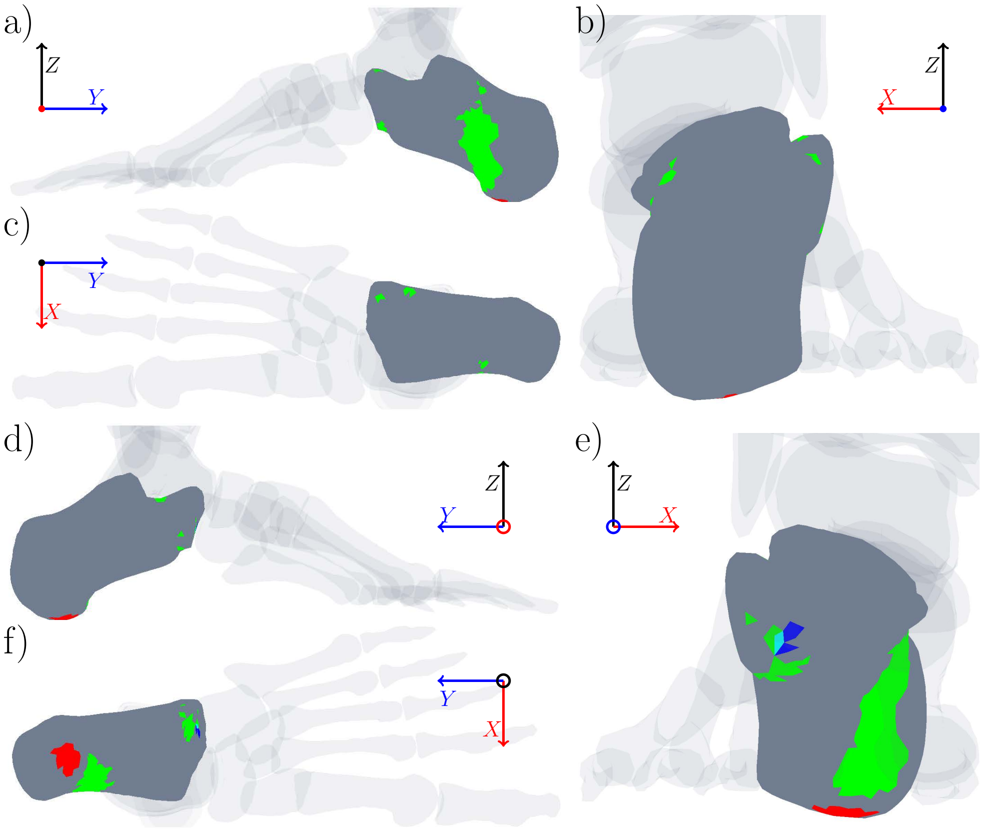

Fig. 11 Stress concentrations of the calcaneus. Red indicates pressures larger than 80 MPa were experienced at that location for a least 1 of the 64 simulations. Blue indicates pressures lower than –80 MPa. Green indicates von Mises stresses larger than 150 MPa. The colors are additive, therefore yellow means that both the green and red conditions have been met, cyan indicates that the blue and green conditions have been met, and black is representative of all 3 conditions. Each panel shows a different view of the foot.

Figure 12 is the analogous figure for showing the stress concentrations for the talus. Panels *b, d*, and *f* show multiple patches of von Mises stress concentrations (green) and combinations of other extremes (blue, yellow, and black) in and around the joint of the 2 bones. Panels *c* and *e* reveal additional patches of elements where the von Mises stresses are large and the pressures are compressive. These regions are located near the calcaneus but also where the talus meets the tibia.

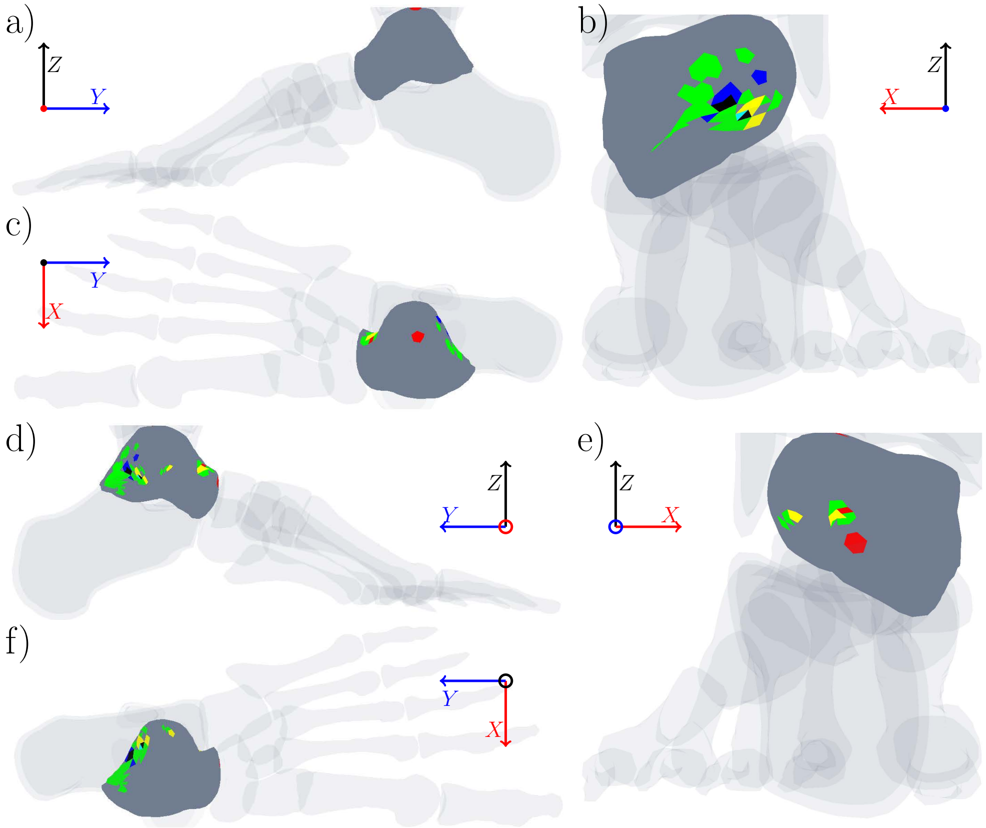

Fig. 12 Stress concentrations of the talus. Red indicates pressures larger than 80 MPa were experienced at that location for a least 1 of the 64 simulations. Blue indicates pressures lower than –80 M Pa. Green indicates von Mises stresses larger than 150 MPa. The colors are additive therefore yellow means that both the green and red conditions have been met, cyan indicates that the blue and green conditions have been met, and black is representative of all 3 conditions. Each panel shows a different view of the foot.

4. Discussion

We conducted 64 simulations on a lower leg finite element model to understand the sensitivity of predicted injury on the choices of material parameters. The same accelerative loading condition was applied to each of the 64 simulations. This work is one of many studies to be conducted on the lower leg and was designed to serve as a baseline for future comparisons. Here we discuss relevant issues that have not been addressed previously in the report. For example, several significant unanswered research questions are as follows: What physical effects are most important for predicting injury? Does injury occur on a strain and time scale where nonlinearity and rate-dependencies are large effects, or can these effects be neglected? Furthermore, have we assumed a sufficient level of detail in our model?

4.1 Biofidelity and Injury Predictive Capability

Throughout the simulation literature, there is a large range of tissue material properties. Here we considered both low and high values reported in the literature for 6 different material parameters. Using combinations of these parameters, we reproduced situations that would be potentially injurious for bones of the lower leg. While we do not actually model failure, there are some clear cases where the concentration of stress would result in element deletion or trigger some other numerical method for failure. In Sections 3.1 and 3.4, we reported that the soft tissue plays a role in the types of injuries predicted. Two questions that still need to be addressed: Why does the soft tissue property directly affect the stress concentrations we see in the cortical shell of a neighboring bone? Have we represented the interfaces adequately in our numerical model?

From our results, we can conclude that injury prediction by itself is not a meaningful metric for validation purposes. Figures 5 and 6 illustrate that by only changing one material parameter we could significantly affect the specific bones that were injured and their severity. Thus, certain combinations of material parameters could selectively produce a different set of injuries. The conundrum lies in that all of the material parameters we simulated were within the accepted range of values, thus each one represented a valid choice in the model and each one predicted different injuries.

Predicted calcaneus and talus injuries were a core focus of our results. In Section 3.1, we reported that the talus was highly susceptible to both pressure and von Mises stress concentrations. This was additionally supported through the historgrams (Figs. 9 and 10, and supplemental figures in Appendix C where the number of talus failures far exceeded calcaneus failures using a von Mises failure criteria, and are on par with calcaneus failures using the pressure criteria. Stress localizations were identified in Figs. 11 and 12 that pointed to the particular interface where injuries typically would occur. Similar fractures of the talus were also observed in Kraft et al.,[16] whose model, despite sharing the same foundation as the current model, contained significant differences as well. For example, the Kraft et al. model included ligaments, rate-dependent constitutive models, fracture criteria for cortical and trabecular bone, and considered an entirely different loading function. Despite these large differences, Kraft et al. also observed talus fractures, even in cases where the calcaneus fractured quite extensively.

However, in comparison with other lower extremity injuries, fractures of the talus are relatively uncommon and are typically the result of high-energy trauma. Talus fractures constitute less than 1% of all reported fractures and only 3% to 6% of all foot fractures.[25,26] Henderson et al. conducted a study in which 18 postmortem human subject (PMHS) lower limbs were subjected to a high rate impact, similar to loads observed in military vehicles. In all of their tests they only saw 3 talus fractures.[3] The accepted injury mechanism of talus fractures is a hyperdorsiflexion force, in which the toes are forced toward the shin beyond their normal range. This causes the posterior ligaments of the subtalar joint (meeting point of the talus and calcaneus) to rupture, the neck of the talus to impact against the leading anterior edge of the distal tibia, and a fracture line to develop.[25,26]

Due to the unrealistic, high number of talus failures we saw in our results, and the localization of the largest stresses occurring between the talus and the calcaneus, we believe that the talus injuries represent a false-positive in our injury predictive capability. It is necessary to revisit and improve the level of detail in our model, specifically in the complex joint structures of the ankle. Since calcaneus injuries were closely related to the soft tissue properties and both talus and calcaneus injuries existed in the original model by Kraft et al., we suspect the oversight in how the joint is modeled is common to both models. As mentioned in Section 2, we represented all the muscles, tendons, ligaments, connective tissue, and skin as one material. This soft tissue is in a tied contact with the bones. Early in the research, shared nodes were used between the soft tissue and the cortical bone. These simulations terminated extremely quickly due to negative volumes, potentially indicating a mesh sensitivity that was only reduced by the definition of contact. In the human body, there are undoubtedly both tied and slip surfaces that exist between bone and cartilage, bone and ligaments/tendons, and bone and muscle. From a mechanics standpoint, the interfaces between soft tissues and bone can be quite challenging to model. True joint structures transition from bone to cartilage to a fluid layer before meeting the neighboring cartilage layer. It is possible that the current contact definition between the cortical bone and the soft tissue is overly restrictive and part of the source of large shear stresses in what one might think is a largely compression-dominated problem. We suspect the homogenization and perhaps (overly) restrictive contact definitions are likely candidates to revisit and improve in our model before further use.

4.2 Physical Considerations

In this section, we provide some estimates using isotropic linear elastic theory that we later use to frame further discussion of our results. Using the small strain theory of linear elasticity, one can estimate the time it takes for an elastic wave to propagate from the foot to the femoral head. The largest acoustic wave speed originates from the cortical bone and is approximately 3,700 m/s (for the theory of linear elasticity see, for example, Landau and Lifshitz[27]). The distance from the calcaneus to the femoral head is approximately 0.9 m, yielding an estimated travel time of 0.24 ms. One can then loosely think of 0.24 ms as a unit of time that it takes the wave front to traverse the model (understanding of course that there is no continuous pathway of cortical bone from the calcaneus to the femur). The longest dimension of the calcaneus is approximately 10 times smaller (0.07 m), and the time it takes a wave to travel this distance is 0.02 ms. Finally, the typical thickness of cortical bone can vary but is between millimeters and centimeters, thus placing the travel times on the order of multiple microseconds. In 3.5 ms, an elastic wave in cortical bone can travel a distance of 13 m, which is about 14 lengths of the leg, 190 calcaneus lengths, and up to thousands of cortical thicknesses. These estimates suggest that at the millisecond time-scale, elastic waves have ample time to traverse the cortical shell thickness and the small bones of the feet numerous times.

Wave propagation within the cortical shell provides insight into only part of the problem. Additionally, the tissues of the body can be thought of in terms of layered media. Brekhovskikh's book[28] treats a number of problems in linear elasticity for layered media. Using simple calculations, one can obtain qualitative details regarding reflection and transmission coefficients for layered tissues of the body. First, consider the much-simplified problem of acoustic waves in 2 semi-infinite planes. At normal incidence, and taking the same material parameter ranges used in our simulations, we can estimate a range in the magnitude of reflection coefficients between the flesh and cortical bone to be 0.82–0.96. Similarly for trabecular and cortical bone, we find a range of magnitudes of the reflection coefficients to be 0.60–0.86. These numbers provide some additional insight into the effects the material parameters can have on transmission and reflection of elastic waves. Next, consider a wave that propagates from a semi-infinite volume of steel followed by a finite thickness of flesh and then into a semi-infinite volume of cortical bone. Calculating the frequency dependence of the transmission coefficient at normal incidence into the bone illustrates the importance of understanding the layered tissues of our problem, since the thickness of the flesh layer heavily influences the transmission coefficient. Assuming for this example a flesh thickness of 6 mm, we make the following observations about the transmission coefficient. For frequencies from ω =0 to $\omega = 0.1$ MHz, the transmission coefficient rapidly falls from a value of 1 to almost 0. For frequencies larger than 0.1 MHz, the periodicity of the solution for the transmission coefficient makes the magnitude of the transmission coefficient cycle between complete transmission and complete suppression. Thus, the thin flesh layer can influence the transmitted wave in a similar way to that of a thin film in optics. Further considerations should be made to understand other multilayer problems, e.g., steel to flesh to cortical bone to trabecular bone or steel to rubber to flesh to cortical bone to trabecular bone, since it is these thin layers that can largely influence the transmitted wave and thus influence the predicted injuries.

The mechanism for injury needs to be better understood to properly assign the appropriate level of detail to the finite element model. Regardless of the mechanism, fracture of the bone tissue will occur within the microstructure and the accumulation of which will have effects on the tissue level. By mechanism we mean the combination of conditions that result in a tissue level accumulation of fracture. Intrinsically, the microstructure of bone tissue would need to exceed a critical strain state. For a volume that is deformed quasi-statically, the critical state would occur in a region of the structure that experienced the largest strains due to geometric or structural features, e.g., a sharp curve or point. The specific location of the fracture would thus largely depend on the structural details of the entire bone and the nature of the load that was applied. Alternatively, the material may fracture due to a combination of dynamic effects, such as elastic waves propagating through the structure, inertial loading, or the extreme case of a shock loading. Ignoring the extreme case of shock, any dynamic fracture, or more accurately large strain states, within our model likely originates from a combination of inertial and wave propagative effects. Rate-dependent constitutive models, whether in the bone or in the flesh, will change transmissive properties in the frequency domain; however, the question remains whether these changes are large enough to alter the observed injury location.

4.3 Constitutive Details and Loading

We return to 2 assumptions that warrant additional discussion: the idealized loading condition and the use of isotropic elastic constitutive models.

The loading condition applied to the lower leg model was originally developed for Kolsky bar simulations and is well documented in Fitzpatrick and Scheidler.[18] In their work, Fitzpatrick and Schiedler concluded that piecewise linear functions with discontinuities in the derivative of applied velocity resulted in large amounts of ringing and high-frequency noise. Thus a high quality simulation result depended on a smooth loading function with continuity in the accelerative terms as well as the velocity. Considering the discussion of layered media in the previous section, and as we move toward rate-dependent constitutive models, control over the high-frequency content and noise that might propagate into the models is highly desirable. We note that the largest amplitude high frequency content of our loading curve corresponds to frequencies 250 Hz and sub-kilohertz (time intervals on the order of milliseconds) which is at least 3 orders of magnitude lower than the periodic behaviors of the transmission coefficient in the MHz regime discussed in Section 4.2.

The results from Fig. 4 show both early time (less than 1 ms) and late time (larger than 1 ms) dependence from specific elements. Oscillations are observed and are most prominent in the bones nearest the steel plate and the frequency of which depended on the material parameters of the flesh. These oscillations at early times have relatively high frequency content and are small in amplitude when compared to the lower frequencies that are larger in amplitude at later times. Although further analysis is needed, we can speculate that the changes in soft tissue properties quantitatively change the transmission coefficient for the layer of cortical bone and selectively suppress portions of the initial transient loading. The lower frequencies at later times are essentially seen as a zero-frequency component and are largely transmitted to the bone regardless of material parameter. However, if we are missing a key feature of the loading by assuming an idealized function, these arguments would no longer hold. For instance, a high-frequency oscillation superimposed on our loading condition might transmit extraordinarily well under one region of the calcaneus compared to another thicker region. Similarly, these arguments may not hold at large strain or in the case of a highly viscoelastic material. For instance, a nonlinear elastic constitutive model for flesh would predict a stiffened elastic moduli in addition to features introduced from the thickness of the flesh layer changing. Another question that arises is whether the loading we impose is overly damaging. The loading is entirely specified, which potentially delivers an unphysical impulse.

Typical models of the bone have included elastic,[24,29] elastic-plastic,[1,21,22,30] and viscoelastic,[20,31,32] along with various failure models and fracture methods. While the loading curves may replicate the rate-dependence from experiments, the unloading curves are rarely taken into account. For a plastic material this return is quite different than a viscoelastic material. Incorporating the wrong physics might simply amount to introducing the same error as not including the rate-dependence in the first place, but this will only be clear through detailed comparisons of the simulations that consider both.

There is utility in assuming the small bones of the lower leg are undergoing a quasi-static deformation. This is supported by Figs. 2, 3, and 4 along with the estimates made earlier in the discussion. If this is the case, the structures of these bones and the nature of the loading would be most critical to properly understand their failure. Once the elastic energy enters the cortical layer, it largely follows the cortical shell since waves see fairly large impedance mismatches between the flesh and cortical bone. This impedance mismatch can delay the peak of loading, similar to what is observed in Fig. 4, and thus play a role in the distribution of stress within specific bones.

In past and current US Army conflicts, lower extremity injuries amount to more than 50% of combat wounds.[7–9] The prevalence of complications, in addition to the greater disability scores seen in patients with foot and ankle injuries, stress the importance of understanding exactly which bones are injured. If a rate-dependent model can change the location of where we see injury, we need to understand and incorporate it into our model. The dominant features we need to understand is the inertial loading, the wave propagation that occurs in the multilayered structures, and the natural structural weaknesses that exist in each of the bones. The latter of which can be understood using component level models.

5. Conclusion

Injury in the human body can occur over multiple length and time scales. It links continuum mechanics to biological processes. Simulations and other modeling approaches necessarily simplify the problem via assumptions. However, significant research questions remain, despite (and in light of) these simplifying assumptions: What physical effects carry the highest order terms and have we made the right assumptions? Does injury occur on a strain and time scale where nonlinearity and rate-dependencies are large effects or can these effects be neglected? Where should we focus our attention; to the variability in the structures and interfaces or to the constitutive modeling of rate-dependent and nonlinear materials? In conclusion, from the results and issues brought up in the discussion, it is imperative that we revisit the structural and interface effects within our model.

6. References

1. Dong L, Zhu F, Jin X, Suresh M, Jiang B, Sevagan G, Cai Y, Li G, Yang KH. Blast effect on the lower extremities and its mitigation: a computational study. Journal of the Mechanical Behavior of Biomedical Materials. 2013;28:111–124.

2. NATO HFM-090 Task Group 25. Test methodology for protection of vehicle occupants against anti-vehicular landmine effects. NATO Research and Technology Organization; 2007. Report No.: RTO-TR-HFM-090.

3. Henderson KA, Bailey AM, Christopher JJ, Brozoski F, Salzar RS. Biomechanical response of the lower leg under high rate loading. In: International Research Council on Biomechanics of Injury; 2013 Sep 11–13; Gothenburg, Sweden.

4. Ramasamy A, Masouros SD, Newell N, Hill AM, Proud WG, Brown KA, Bull AMJ, Clasper JC. In-vehicle extremity injuries from improvised explosive devices: current and future foci. Philosophical Transactions of the Royal Society B: Biological Sciences. 2011;366(1562):160–170.

5. Ramasamy A, Hill AM, Masouros S, Gibb I, Bull AMJ, Clasper JC. Blast-related fracture patterns: a forensic biomechanical approach. Journal of the Royal Society Interface. 2011;8(58):689–698.

6. Alvarez CJ. Epidemiology of blast injuries in current operations. NATO Research and Technology Organization; 2011. Report No.: RTO-MP-HFM-207.

7. Tintle SM, Keeling JJ, Shawen SB. Combat foot and ankle trauma. Journal of Surgical Orthopaedic Advances. 2010;19(1):70–76.

8. Ramasamy A, Hill AM, Phillip R, Gibb I, Bull AM, Clasper JC. The modern "deck-slap" injury-calcaneal blast fractures form vehicle explosions. The Journal of Trauma. 2011;71(6):1694–1698.

9. Owens BD, Kragh JF, Macaitis J, Svoboda SJ, Wenke JC. Characterization of extremity wounds in Operation Iraqi Freedom and Operation Enduring Freedom. Journal of Orthopaedic Trauma. 2007;21:254–257.

10. Shawen SB, Keeling JJ, Branstetter J, Kirk KL, Ficke JR. The mangled foot and leg: salvage versus amputation. Foot and Ankle Clinics of North America. 2010;15(1):63–75.

11. NATO HFM-089 Task Group 24. Test methodologies for personal protective equipment against anti-personnel mine blast. NATO Research and Technology Organization; 2004. Report No.: RTO-TR-HRM-089.

12. Footner MJ, Bergeron DM, Swinton RJ. Development and calibration of a frangible leg instrumented for compression and bending. Defence Science and Technology Organization; 2006. Report No.: DSTO-TR-1829.

13. Bergeron DM, Coley GG, Fall R, Anderson IB. Assessment of lower leg injury from land mine blast-phase 2. Defence Research and Development Canada; 2007. Report No.: DRDC Suffield TR 2007-070.

14. Bailey AM, Christopher JJ, Henderson K, Brozoski F, Salzar RS. Comparison of Hybrid-III and PMHS response to simulated underbody blast loading conditions. In: International Research Council on Biomechanics of Injury; 2013 Sep 11–13; Gothenburg, Sweden.

15. Newell N, Masouros SD, Bull AM. A comparison of Mil-Lx and Hybrid-III responses in seated and standing postures with blast mats in simulated under-vehicle explosions. In: International Research Council on Biomechanics of Injury; 2013 Sep 11–13; Gothenburg, Sweden.

16. Kraft RH, Lynch ML, Vogel EWI. Computational failure modeling of lower extremities. Paper presented at: Proceedings of the RTO Human Factors and Medicine Panel (HFM) Symposium. 2011 Oct 3–5; Halifax, Canada.

17. Cheung JTM, Zhang M, Leung AKL, Fan YB. Three-dimensional finite element analysis of the foot during standing– a material sensitivity study. Journal of Biomechanics. 2005;38:1045–1054.

18. Fitzpatrick J, Scheidler M. Considerations for numerical modeling of dynamic behavior of soft materials. In: Chalivendra V, Song B, Casem D, editors. Dynamic Behavior of Materials, Volume 1. Proceedings of the 2012 Annual Con-

ference on Experimental and Applied Mechanics; 2012 June 11–14; Costa Mesa, CA. New York (NY): Springer; 2012.

19. Dohrmann C, Heinstein M, Jung J, Key S, Witkowski W. Node-based uniform strain elements for three-node triangular and four-node tetrahedral meshes. International Journal for Numerical Methods in Engineering. 2000;47(9):1549–1568.
20. Bandak F, Tannous R, Toridis T. On the development of an osseo-ligamentous finite element model of the human ankle joint. International Journal of Solids and Structures. 2001;38(10):1681–1697.
21. Untaroiu C, Darvish K, Crandall J, Deng B, Wang JT. A finite element model of the lower limb for simulation pedestrian impacts. Stapp Car Crash Journal. 2005;49:157–181.
22. Shin J, Yue N, Untaroiu CD. A finite element model of the foot and ankle for automotive impact applications. Annals of Biomedical Engineering. 2012;40(12):2519–2531.
23. Iwamoto M, Omori K, Kimpara H, Nakahira Y, Tamura A, Watanabe I, Miki K, Hasegawa J, Oshita F, Nagakute A. Recent advances in THUMS: development of individual internal organs, brain, small female and pedestrian model. In: Proceedings of 4th European LS-DYNA Users Conference; 2003 May 22–23; Ulm, Germany. p. 1–10.
24. Schuster PJ, Chou CC, Prasad P, Jayaraman G. Development and validation of a pedestrian lower limb non-linear 3-d finite element model. Stapp Car Crash Journal. 2000;44:315–334.
25. Lin S, Hak DJ. Management of talar neck fractures. Trauma Update. 2011;34(9):715–721.
26. Sanders DW. Fractures of the talus. In: Bucholz RW, Heckman JD, Court-Brown C, editors. Rockwood and Green's fractures in adults; 6th ed.; Philadelphia (PA): Lippincott Williams and Wilkins; 2006; p. 2249–2292.
27. Landau LD, Lifshitz EM. Theory of elasticity. 3rd ed. Burlington (MA): Elsevier; 1986.

28. Brekhovskikh L. Waves in layered media. In: Vol. 6 of applied mathematics and mechanics. New York (NY): Academic Press; 1960.

29. Depalle B, Chapurlat R, Walter-Le-Berre H, Bou-Saïd B, Follet H. Finite element dependence of stress evaluation for human trabecular bone. Journal of the Mechanical Behavior of Biomedical Materials. 2013;18:200–212.

30. Mullins LP, Bruzzi MS, McHugh PE. Calibration of a constitutive model for the post-yield behaviour of cortical bone. Journal of the Mechanical Behavior of Biomedical Materials. 2009;2(5):460–470.

31. Natali AN, Carniel E, Pavan PG. Constitutive modelling of inelastic behaviour of cortical bone. Medical Engineering & Physics. 2008;30:905–912.

32. Li Z, Zou D, Liu N, Zhong L, Shao Y, Wan L, Huang P, Chen Y. Finite element analysis of pedestrian lower limb fractures by direct force: the result of being run over or impact? Forensic Science International. 2013;229(1):43–51.

Appendix A. Details of the Numerical Simulation

Surface geometries for the anatomical mesh were obtained from Zygote Media Group, Inc. in Wavefront .obj format. These surface geometries were created and "typified" from CT (computer tomography) and MRI (magnetic resonance imaging) scans of human male subjects who anthropomorphically fit within the 50th percentile. The geometries used for this model include the exterior surfaces of the skin, the 26 bones of the foot, the patella, and the long bones of the leg. The bones and skin were initially in the standing position. To make the seated position, the femur was rotated 90° in the sagittal plane and then visually adjusted in the frontal and transverse planes so that the femoral condyles sat nicely on the tibial plateau. The position of the patella was also adjusted in similar fashion. The skin required manual sculpting and patching to bend at the knee and hips.

Differentiation between cortical and trabecular bone types was achieved by duplicating, downscaling, manually sculpting, and nesting bone geometries to create the cortical layer; the void space between the inner scaled bone and the original outer bone was considered the cortical shell. Thus, a sharp interface exists, as there is no transition zone from cortical to trabecular bone. Appropriate relative cortical thickness was sought between the diaphysis and epiphyses of the long bones (i.e., thicker in the diaphysis, thinner in the epiphyses). However, no data were used to substantiate this effort. Also, the inner bone structure of the patella, talus, and calcaneus is not well understood, and therefore a uniformly thick cortical shell was used. The model also does not include geometry for a medullary cavity; the interior of each bone below the cortical layer in its entirety is considered to be the trabecular bone region. Bones in the mid-and forefoot do not have cortical-trabecular bone differentiation and are assigned cortical bone properties.

All manipulation described to this point was done in Blender (V2.49, Amsterdam, Netherlands). Stereolithography (STL) files were exported from Blender and brought into the meshing software ICEM CFD (V15; ANSYS, Canonsburg, PA). Further geometry manipulation was performed in ICEM CFD; the middle and distal phalanges of the toes were shrink-wrapped so they were fused together. Everything was then meshed simultaneously, hence the nodes between different component parts are shared (i.e., between cortical and trabecular bone, cortical bone, and surrounding flesh).

The model was then exported from ICEM CFD in LS-Dyna format and opened in LS-PrePost (V4.0, LSTC, Lawrence Livermore National Laboratory). Mesh manipulation was performed here, which included cleaning up stray elements that would connect neighboring bones; these elements were manually selected and reassigned to the surrounding flesh. Hence, each bone in the model is isolated from any surrounding bones via a flesh buffer. A flat plate of hexahedral elements was created in LS-PrePost and centered under the feet. The model was then initialized in LS-Dyna version 6.1.0 to bring the bottom of the feet flat and in contact with the plate. This included applying a velocity of 0.5 m/s to the plate in the upward (Z) direction toward the feet. Once the bottom of the heel contacted the plate, the nodal coordinates of the model at that state were saved and exported. Next, a new instance of the original model was opened in LS-PrePost, and the initialized state coordinates were imported without offset to rewrite the nodal coordinates of the original model. For this work, the left leg and pelvis were removed from the model, leaving the right leg. The flesh was removed just above midfemur; the entire right femur itself remained intact. A jagged mesh at the site of flesh deletion remained and was cleaned up by hand by creating elements from nodes on the exposed face of the flesh.

To run the model in Sierra/SolidMechanics, the mesh needed to be in Exodus file format, which LS-PrePost cannot directly export. Hence, the model was converted to an Exodus file format through the use of HyperMesh (V12.0; Altair) and Cubit (V13.1; Sandia National Laboratory); the model was exported in LS-Dyna format from LS-PrePost, imported into HyperMesh, exported as an Abaqus .inp file, imported into Cubit, and then exported as an Exodus .g file. Tied contact was used between the flesh and bones.

The model contains approximately a half million tetrahedral elements. The typical criticism of the tetrahedron element is volumetric locking for materials with a large Poisson's ratio. The large values of Poisson's ratio of the flesh would certainly cause locking in the traditional tet element. As a result, we are using a nodal-based tet[1]. For bend tests this nodal-based tet did not suffer from volumetric locking for Poisson's ratios as high as 0.49. While they do not always perform as well

---

[1] Dohrmann C, Heinstein M, Jung J, Key S, Witkowski W. Node-based uniform strain elements for three-node triangular and four-node tetrahedral meshes. International Journal for Numerical Methods in Engineering. 2000;47(9):1549–1568.

as a traditional hexahedral element, given the complicated geometry of the flesh, they were the best available option. A rate integrated formulation of a linear elastic material was used in SIERRA for all anatomical components. Typical stresses observed in the bones were small compared to the elastic moduli, thus implying that strains were also small.

Postprocessing of simulation results was carried out in ParaView (V3.14.0; Kitware), SEACAS (Sandia National Laboratory), EnSight (v10.0.3c; CEI, Inc., Apex, NC), and MATLAB (The MathWorks, Natick, MA).

Appendix B. Mathematical Formulation of a Smooth Loading Pulse

For all of the simulations of the lower leg, we require a loading pulse (i.e., an applied velocity history v) that ramps up smoothly to a constant value before subsequently unloading (Fig. 1c in report). In this appendix we formulate a parameterized loading pulse using a Hermitian smoothing spline.

We use a Hermitian smoothing spline of degree 5 as the basis for the ramp-up portion of the loading pulse[1]):

$$\mathbf{H}_5(x) = 10x^3 - 15x^4 + 6x^5, \quad 0 \le x \le 1\,. \tag{B-1}$$

This function increases from 0 at $x = 0$ to 1 at $x = 1$, and has zero first and second derivatives at both of these end points. Following Fitzpatrick and Scheidler[1] (without loss of generality letting strain-rate become velocity v and strain becomes displacement δ), one can use $\mathbf{H}_5(x)$ to construct a velocity function that ramps up from 0 to v_{max} over the time interval $[\,0\,, t_r\,]$, maintains this constant value over the time interval $[\,t_r\,, t_r + t_p\,]$, and then unloads to zero over the time interval $[\,t_r + t_p\,, t_d\,]$:

$$v(t) = \begin{cases} 0, & t < 0 \\ v_{\text{max}}\,\mathbf{H}_5\!\left(\frac{t}{t_r}\right), & 0 \le t \le t_r \\ v_{\text{max}}, & t_r < t < t_r + t_p \\ v_{\text{max}}\left[1 - \mathbf{H}_5\!\left(\frac{t-(t_r+t_p)}{t_r}\right)\right], & t_r + t_p \le t \le t_d \\ 0, & t > t_d\,. \end{cases} \tag{B-2}$$

t_r is referred to as the rise time (i.e., the time it takes to reach a constant velocity), t_p is the duration of the constant velocity plateau, and t_d is the total duration of the pulse. In the simulations, we made the additional assumption that the loading pulse is symmetric; therefore, the unloading duration $t_d - (t_r + t_p)$ equals the rise time, so that $t_d = 2\,t_r + t_p$.

---

[1] Fitzpatrick J, Scheidler M. Considerations for numerical modeling of dynamic behavior of soft materials. In: Chalivendra V, Song B, Casem D, editors. Dynamic Behavior of Materials, Volume 1. Proceedings of the 2012 Annual Conference on Experimental and Applied Mechanics; 2012 June 11–14; Costa Mesa, CA. New York (NY): Springer; 2012.

Note that

$$\dot{v}(0) = \dot{v}(t_r) = \dot{v}(t_r + t_p) = 0 \tag{B-3}$$

and

$$\ddot{v}(0) = \ddot{v}(t_r) = \ddot{v}(t_r + t_p) = 0\,. \tag{B-4}$$

Since $\dot{v}$ and $\ddot{v}$ are identically zero during the constant velocity plateau, as well as for $t < 0$ and $t > t_d$, the conditions in Eqs. B-3 and B-4 guarantee that v is twice continuously differentiable. This degree of smoothness was necessary to avoid an unwanted ringing in the simulations that would otherwise result from a lower order polynomial.

An explicit expression for $\delta(t)$ is rather messy, and in practice it is simpler to work with the integral of $\mathbb{H}_5$:

$$\mathbb{H}_5(x) = \int_0^x \mathbf{H}_5(y)\,\mathrm{d}y = x^4\left(x^2 - 3x + \frac{5}{2}\right)\,. \tag{B-5}$$

Integrating each case in Eq. B-2 with respect to time, assuming a symmetric loading pulse, and using $\mathbb{H}_5(1) = 1/2$, gives:

$$\delta(t) = \begin{cases} 0, & t < 0 \\ v_{\max}\, t_r\, \mathbb{H}_5(\frac{t}{t_r}), & 0 \le t \le t_r \\ v_{\max}\left[t_r/2 + (t - t_r)\right], & t_r < t < t_r + t_p \\ v_{\max}\left[t_r/2 + (t - t_r) - t_r\, \mathbb{H}_5\big(\frac{t-(t_r+t_p)}{t_r}\big)\right], & t_r + t_p \le t \le 2t_r + t_p \\ v_{\max}\left[t_r + t_p\right], & t > 2t_r + t_p = t_d\,. \end{cases} \tag{B-6}$$

INTENTIONALLY LEFT BLANK.

Appendix C. Failure Criteria Figures

Failure occurrences are tallied at various bones for a range of thresholds. Each panel is specific to an individual bone and tallies the number of simulations for which the absolute value of the pressure within any element in the bone exceeded the damage threshold. The bar colors indicate which damage threshold the tally corresponds to. Low and high values for the material parameter as well as the specific damage thresholds used are indicated on the right under the key. Figures C-1 through C-5 look at a pressure-based failure criteria. Figures C-6 through C-10 look at a von Mises-based failure criteria.

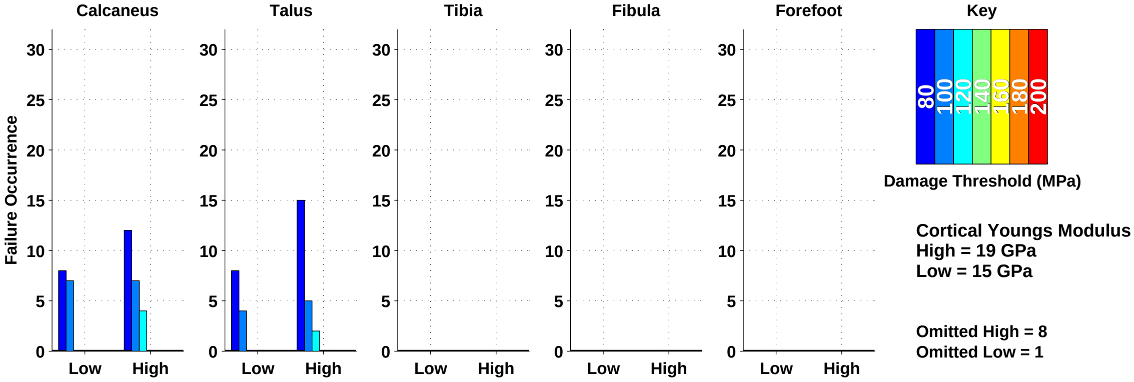

Fig. C-1 Excessive pressure failure occurrence seen in each bone by varying the Young's modulus of cortical bone

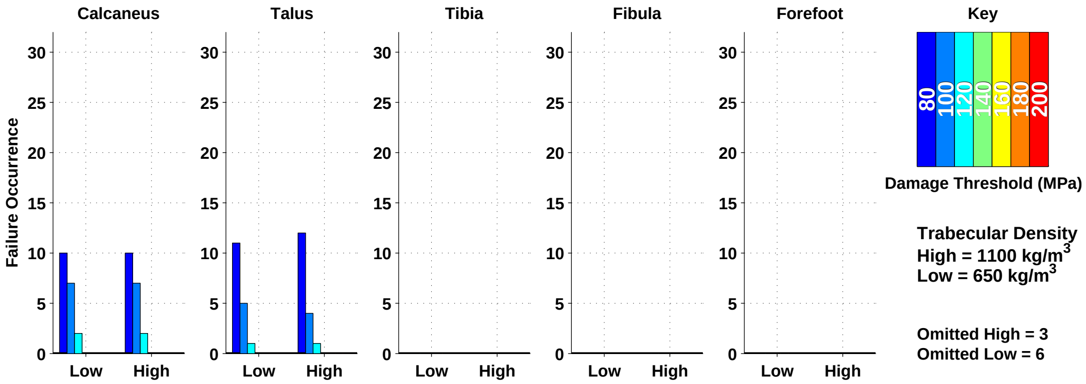

Fig. C-2 Excessive pressure failure occurrence seen in each bone by varying the density of trabecular bone

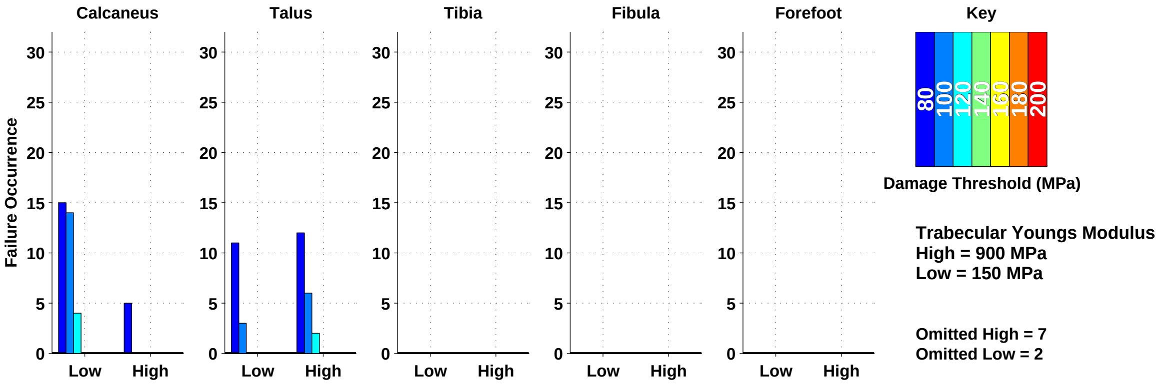

Fig. C-3 Excessive pressure failure occurrence seen in each bone by varying the Young's modulus of trabecular bone

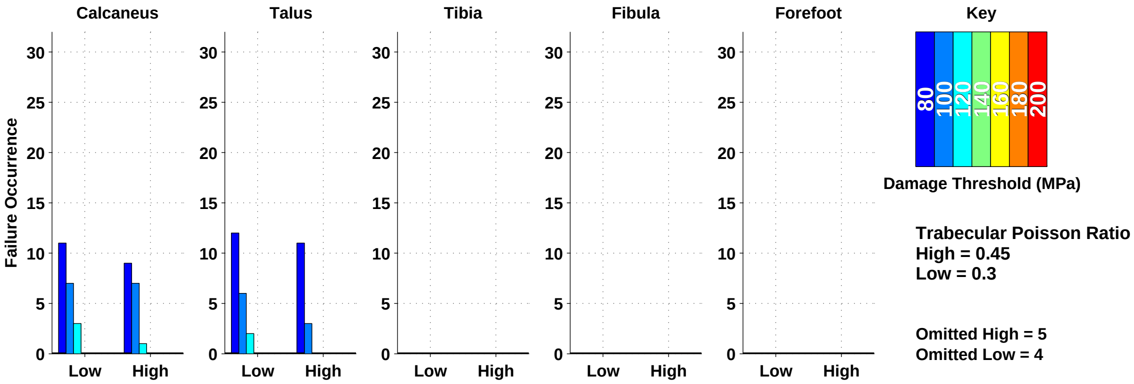

Fig. C-4 Excessive pressure failure occurrence seen in each bone by varying the Poisson's ratio of trabecular bone

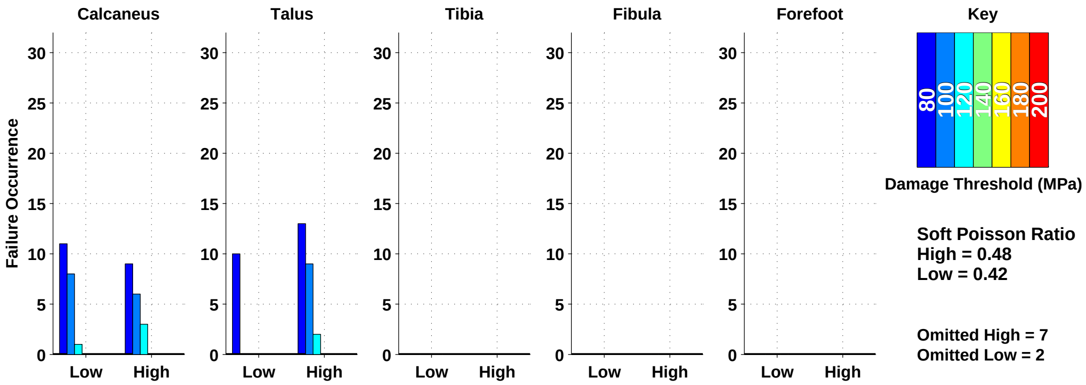

Fig. C-5 Excessive pressure failure occurrence seen in each bone by varying the Poisson's ratio of flesh

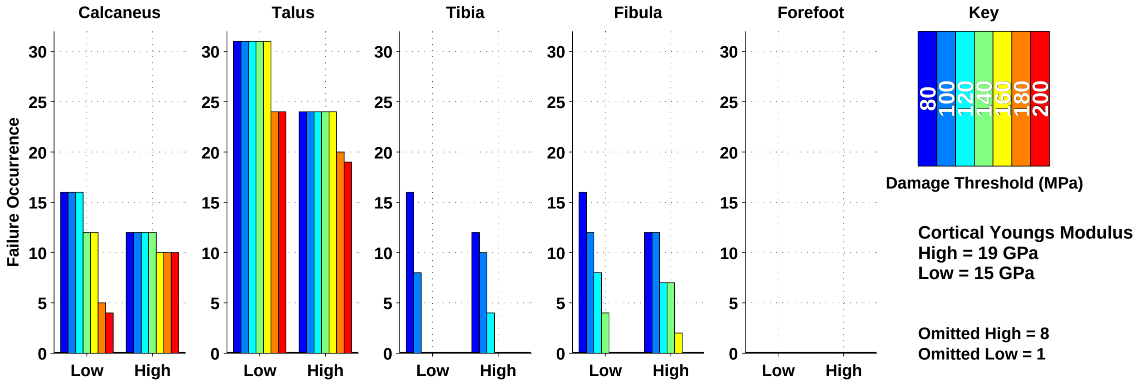

Fig. C-6 Excessive von Mises failure occurrence seen in each bone by varying the Young's modulus of cortical bone

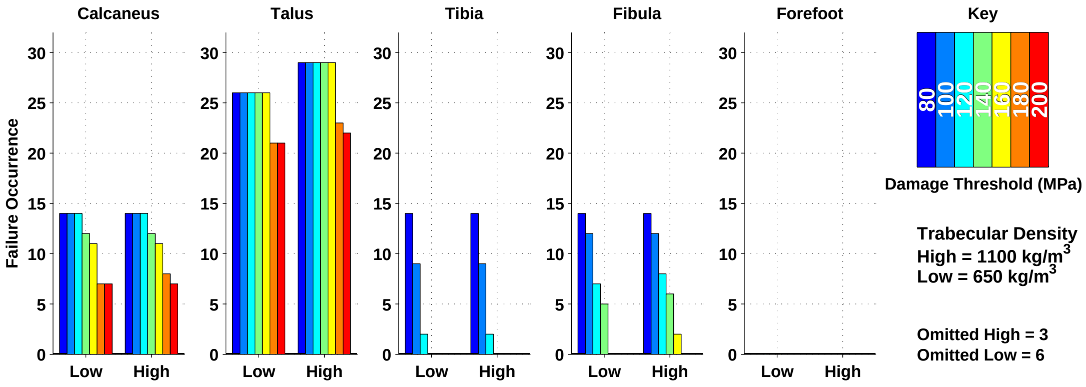

Fig. C-7 Excessive von Mises failure occurrence seen in each bone by varying the density of trabecular bone

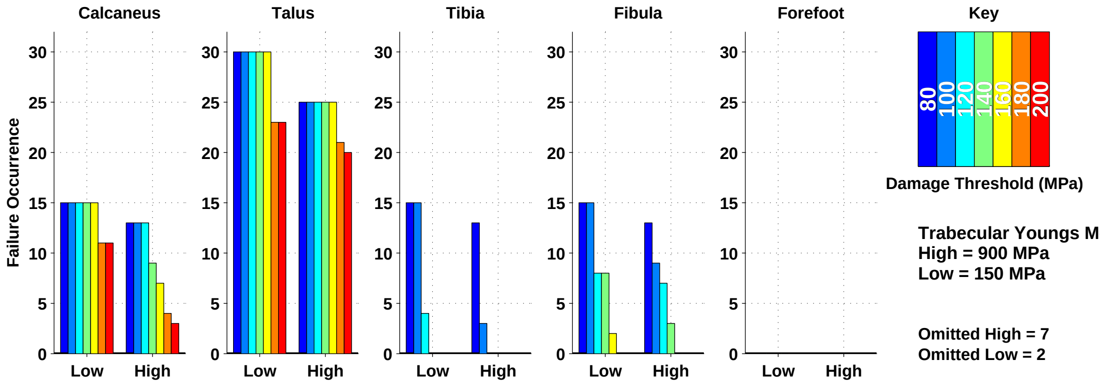

Trabecular Youngs Modulus
High = 900 MPa
Low = 150 MPa

Omitted High = 7
Omitted Low = 2

Fig. C-8 Excessive von Mises failure occurrence seen in each bone by varying the Young's modulus of trabecular bone

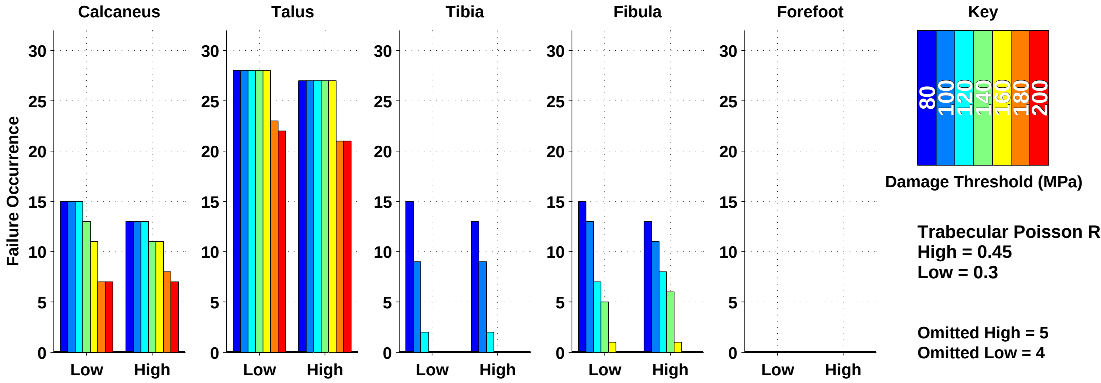

Trabecular Poisson Ratio
High = 0.45
Low = 0.3

Omitted High = 5
Omitted Low = 4

Fig. C-9 Excessive von Mises failure occurrence seen in each bone by varying the Poisson's ratio of trabecular bone

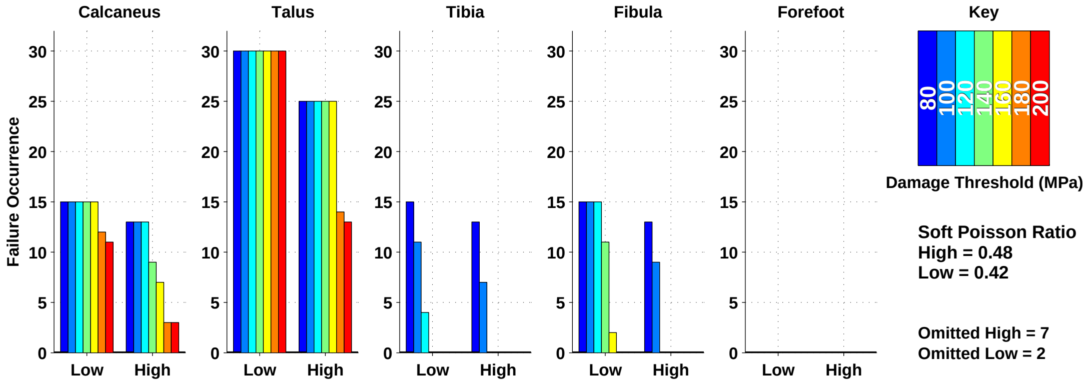

Soft Poisson Ratio
High = 0.48
Low = 0.42

Omitted High = 7
Omitted Low = 2

Fig. C-10 Excessive von Mises failure occurrence seen in each bone by varying the Poisson's ratio of flesh

1 DEFENSE TECHNICAL
(PDF) INFORMATION CTR
DTIC OCA

2 DIRECTOR
(PDF) US ARMY RESEARCH LAB
RDRL CIO LL
IMAL HRA MAIL & RECORDS MGMT

1 GOVT PRINTG OFC
(PDF) A MALHOTRA

67 DIR USARL
(PDF) RDRL CIH C
A BREUER
B HENZ
M VINDIOLA
RDRL DPW
R COATES
P FROUNFELKER
R SPINK
M TEGTMEYER
RDRL HR
P FRANASZCZUK
RDRL HRS
K OIE
RDRL HRS C
S GORDON
W HAIRSTON
B LANCE
K MCDOWELL
A PASSARO
M PETERSON
J VETTEL
RDRL ROP L
F GREGORY
RDRL SLB W
D BOOTHE
N EBERIUS
P GILLICH
C KENNEDY
A KULAGA
W MERMAGEN
RDRL WM
S KARNA
RDRL WML C
T PIEHLER
RDRL WML H
B SCHUSTER
RDRL WMM B
B LOVE
M LYNCH
RDRL WMM G
L PIEHLER
N ZANDER
RDRL WMP
S SCHOENFELD
RDRL WMP B
S ALEXANDER
A DAGRO
A DILEONARDI
W EVANS
C GUNNARSSON
C HAMPTON
C HOPPEL
Y HUANG
M KLEINBERGER
J MCDONALD
A MORGAN
P MCKEE
S SATAPATHY
A SOKOLOW
C WEAVER
T WEERASOORIYA
S WOZNIAK
T ZHANG
K ZIEGLER
RDRL WMP C
S BILYK
T BJERKE
D CASEM
J CLAYTON
D DANDEKAR
M GREENFIELD
B LEAVY
RDRL WMP D
R DONEY
J RUNYEON
RDRL WMP E
P SWOBODA
RDRL WMP F
E FIORAVANTE
N GNIAZDOWSKI
R GUPTA
R KARGUS
RDRL WMP G
R BANTON
N ELDREDGE
S KUKUCK